Thermo-Mechanical Finite-Element Model of Shell Behavior In Continuous Casting of Steel

CHUNSHENG LI and BRIAN G. THOMAS

Mechanical and Industrial Engineering Department

University of Illinois at Urbana-Champaign

Urbana, IL 61801

Ph: 217-333-6919; Fax: 217-244-6534; Email: bgthomas@uiuc.edu

A coupled finite-element model, CON2D, has been developed to simulate temperature, stress, and shape development during the continuous casting of steel, both in and below the mold. The model simulates a transverse section of the strand in generalized plane strain as it moves down at the casting speed. It includes the effects of heat conduction, solidification, non-uniform superheat dissipation due to turbulent fluid flow, mutual dependence of the heat transfer and shrinkage on the size of the interfacial gap, taper and thermal distortion of the mold. The stress model features an elastic-viscoplastic creep constitutive equation that accounts for the different responses of the liquid, semi-solid, delta-ferrite, and austenite phases. Functions depending on temperature and composition are employed for properties such as thermal linear expansion. A contact algorithm is used to prevent penetration of the shell into the mold wall due to the internal liquid pressure. An efficient two-step algorithm is used to integrate these highly non-linear equations. The model is validated with an analytical solution for both temperature and stress in a solidifying slab. It is applied to simulate continuous casting of a 120mm billet and compares favorably with plant measurements of mold wall temperature, total heat removal and shell thickness, including thinning of the corner. The model is ready to investigate issues in continuous casting such as mold taper optimization, minimum shell thickness to avoid breakouts, and maximum casting speed to avoid hot tear crack formation due to submold bulging.

I. INTRODUCTION

Computational models are important tools to gain insight into thermal and mechanical behavior during complex manufacturing processes such as the continuous casting of steel billets. This process features many interacting phenomena which challenge modeling methods, shown in Figure 1(a). Starting with the turbulent flow of molten steel into the mold cavity, superheat is dissipated during flow recirculation in the liquid pool prior to solidifying a shell against the walls of a water cooled copper mold. Heat transfer is controlled by conduction through the solidifying steel shell, the mold and especially the size and properties of the interfacial layers between them. After initial solidification at the meniscus, the shell tends to shrink away from the mold walls due to thermal contraction. Over most of the strand surface, internal "ferrostatic pressure" from the head of molten metal maintains good contact between the shell and the mold. However, shrinkage near the corners may create gaps or intermittent contact, which greatly lowers the local cooling rate. The extent of the gap depends on the composition-dependent shrinkage of the steel shell, its creep resistance, the casting speed, taper and thermal distortion of the mold walls and the thermal properties of the material filling the interfacial gap. The mechanical behavior of the shell also controls the formation of defects such as hot-tear cracks and breakouts, and depends on thermal shrinkage, high-temperature inelastic stress generation rate, solid-state phase transformations, temperature, steel composition, multidimensional stress state and deformation rate. The harsh environment of the steel plant makes it difficult to conduct experiments during the process. To improve insight into these phenomena demands sophisticated mathematical models, to aid the traditional tools of physical models, lab, and plant experiments.

A thermal-mechanical finite-element model that incorporates the above phenomena, CON2D, has been developed in the Metals Processing Simulation Laboratory at UIUC over the past decade [1-4] with several applications [5-12]. After a brief literature review, this paper describes the features of the CON2D model. It then presents its validation with analytical solutions and a simulation of a continuous steel billet casting process where plant measurements were available for comparison.

II. PREVIOUS WORK

Many previous computational models have investigated thermal stress during the continuous casting of steel including models of billet casting [13-19], beam blanks[20], slab casting [2, 6, 11, 13, 14, 21-31], and thin-slab casting [32-34]. Brimacombe, Grill, and coworkers first applied computational thermal stress models of a 2-D billet section under plain stress [13, 14] as it moved down the caster. These and similar early models [21-23] revealed important insights into crack formation, such as the need to avoid reheating. This infant stage of computational stress modeling was qualitative due to the lack of material properties at high temperature, a simple elastic-plastic constitutive model, and course meshes due to computer limitations.

Rammerstorfer et. al. added a separate creep function in developing a thermo-visco-elastic-plastic stress model of a transient 1-D slice domain through a slab [24]. Kristiansson [15] advanced the traveling slice model with stepwise coupling of the thermal and stress computations within a 2-D billet section, based on the interfacial gap between the mold and shell. This model also featured different creep constants for modeling austenite and δ-ferrite, and temperature-dependent properties. Similar models were developed for slab sections [26], including some that assumed plane strain [27]. Kelly *et. al.* [16] developed an axisymmetric model of coupled thermal stress in round billets to study the effect of carbon content on the formation of longitudinal cracks. Elastic stress analysis was performed on the mold and the billet to determine the interfacial gap profile, followed by elastic-plastic stress analysis of the billet.

Recently, several improved models have been developed of thermal-mechanical behavior of continuous-cast steel. Boehmer et. al. [17] coupled a 3-D in-house heat flow model and 2-D thermal stress model in ADINA, to analyze a continuous-cast billet section in plane stress. An elastoplastic constitutive model was adopted including strain-rate dependent strength and plasticity, and a separate creep model, if necessary. The solidifying solid was discretized with a deforming grid and liquid elements were deleted from the stress simulation.

A transverse slice model, AMEC2D, was developed to simulate beam-blank casting, including elastic-viscoplastic behavior and a simple fluid flow model to account for superheat transport in the liquid pool [20]. Park et al. applied AMEC2D to investigate the effect of mold corner radius on shell growth and longitudinal corner cracks in billets [18]. This model assumed plane stress and neglected the effects of superheat variations.

Fachinotti *et. al.* developed Arbitrary Lagrangian Eulerian (ALE) [31] and mixed Eulerian-Lagrangian [19] thermal mechanical models, to analyze stress/strain distributions in continuous-cast round steel billets. These rigorous models adopt elastic-viscoplastic material behavior with temperature and history dependent material parameters, but are computationally intensive and assume 2-D axisymmetry. They show that the generalized plane strain assumption matches closest to the real behavior, short of a full 3-D analysis.

Many important related aspects of continuous casting have been modeled in depth and are discussed elsewhere [35, 36], including fluid flow in the molten steel pool [37], nonequilibrium solidification of the shell [35] [38], thermal distortion of the mold [39], bulging and bending of the strand below the mold [40, 41] and crack prediction [35] [42].

Although they have generated important insights, previous thermal-mechanical models of shell solidification in the mold still oversimplify some phenomena or are too computationally expensive to simulate large scale problems with sufficient mesh and time step refinement to be accurate. There is still a need for better models to gain more quantitative insight into thermal-mechanical behavior and crack prediction in continuous casting of steel.

III. GOVERNING EQUATIONS

The model solves the transient heat conduction equation and corresponding force equilibrium equation for temperature, displacement, strain, and stress in a transverse Lagrangian reference frame moving downward with the steel shell at the casting speed, as shown in Figure 1(a). Both 2-D and 1-D slice domains are simulated, as shown in Figure 1(b) and (c) respectively.

A. Heat Transfer and Solidification Model

The model first solves the transient energy balance Eq. [1], where *H(T)* and *k(T)* are isotropic temperature dependent enthalpy and conductivity [43].

$$\rho \frac{\partial H(T)}{\partial T} = \nabla \cdot \left(k(T) \nabla T \right) \qquad [1]$$

A 2-D simplification of the full 3-D process is reasonable because axial (z-direction) heat conduction is negligible relative to advection at the high Péclet number of this steel continuous casting process ($vL/\alpha = 2098$ [1]).

Applying the chain rule to the left hand side of Eq. [1] isolates the specific heat, c_p, and latent heat, L_f, together in a convenient function, $\partial H(T)/\partial T$, in Eq. [2]. Heat balance numerical errors are lessened by providing an enthalpy-temperature look-up function.

$$\rho \left(\frac{\partial H(T)}{\partial T} \right) \left(\frac{\partial T}{\partial t} \right) = \frac{\partial}{\partial x} \left(k(T) \frac{\partial T}{\partial x} \right) + \frac{\partial}{\partial y} \left(k(T) \frac{\partial T}{\partial y} \right) \qquad [2]$$

Boundary conditions can be fixed temperature, heat flux, convection, or a heat resistor model across the interfacial layer between the mold wall and the steel surface [43]. The latter enables the fully coupled heat transfer and stress analysis described in Section VII-C. The thermal property functions of steels, including conductivity and enthalpy, are given in Section X-B.

B. Stress Model

The general governing equation for the static mechanics problem in this Lagrangian frame is given by the force equilibrium balance in Eq. [3] [44].

$$\nabla \cdot \underset{\approx}{\sigma} + \rho \underset{\sim}{b} = \underset{\sim}{0} \qquad [3]$$

Below the meniscus region, axial temperature gradients and the corresponding displacement gradients are generally small, so it is reasonable to apply a generalized plane

---

[1] $v = 0.0167(m/\sec)$, $L = 1(m)$, $\rho = 7500(kg/m^3)$, $c_p = 0.6(kJ/kgK)$, $K = 40(W/mK)$

strain assumption in the casting direction. This enables a 2-D transient stress analysis to provide a reasonable approximation of the complete 3-D stress state. Although this is not quite as accurate as a fully 3-D analysis [31], this slice model approach can realistically model the entire continuous casting process, with the possible exception of the meniscus region, at a relatively small computational cost.

The incremental governing equations acting over each time step, Δt, for the generalized plane strain condition, simplify Eq. [3] to the following:

$$\begin{aligned}
&\frac{\partial \Delta \sigma_x}{\partial x} + \frac{\partial \Delta \tau_{xy}}{\partial y} = 0 \\
&\frac{\partial \Delta \sigma_y}{\partial y} + \frac{\partial \Delta \tau_{xy}}{\partial x} = 0 \\
&\int \Delta \sigma_z dA = \Delta F_z \\
&\int x \Delta \sigma_z dA = \Delta M_x \\
&\int y \Delta \sigma_z dA = \Delta M_y
\end{aligned} \qquad [4]$$

Incremental total strains $\{\Delta\varepsilon\}$ are related to displacements $\{u_x, u_y, u_z\}$ according to Eq. [5].

$$\begin{aligned}
&\Delta \varepsilon_x = \frac{\partial \Delta u_x}{\partial x} \\
&\Delta \varepsilon_y = \frac{\partial \Delta u_y}{\partial y} \\
&\Delta \varepsilon_{xy} = \frac{1}{2}\left(\frac{\partial \Delta u_y}{\partial x} + \frac{\partial \Delta u_x}{\partial y} \right) \\
&\Delta \varepsilon_z = a + bx + cy
\end{aligned} \qquad [5]$$

There are no body forces because the ferrostatic pressure caused by gravity acting on the liquid is instead applied through internal boundary conditions described in Section IX-B. Besides the regular boundary conditions like fixed displacements and surface tractions, a special type of boundary, mold wall constraint, is included in CON2D to model the interactions between the mold wall and the steel surface, as addressed in Section VIII-B. The distorted shape of the mold has an important influence on the size of the interfacial gap, heat transfer, and consequently stress, so is incorporated as discussed in Section VIII-A.

Two fold symmetry can be assumed in the current continuous casting application, so the constants related to bending, b and c in Eq. [5] and ΔM_x and ΔM_y in Eq. [4] all vanish and $\Delta\varepsilon_Z$ represents the unconstrained axial (thickness) contraction of each 2-D slice.

IV. CONSTITUTIVE MODELS

Increments of stress and elastic strain are related through Hook's Law, Eq. [6]. Matrix $[D]$ contains the isotropic temperature-dependent elastic modulus, $E(T)$, and Poisson's ratio, υ, given in Eq. [7].

$$\{\Delta\sigma\} = [D]\{\Delta\varepsilon_e\} + [\Delta D]\{\varepsilon_e\} \qquad [6]$$

where $\{\sigma\} = \{\sigma_x \quad \sigma_y \quad \tau_{xy} \quad \sigma_z\}^T \qquad \{\varepsilon\} = \{\varepsilon_x \quad \varepsilon_y \quad \varepsilon_{xy} \quad \varepsilon_z\}^T$

$$[D] = \frac{E(T)}{(1+\nu)(1-2\nu)} \begin{bmatrix} 1-\nu & \nu & 0 & \nu \\ \nu & 1-\nu & 0 & \nu \\ 0 & 0 & \frac{1-2\nu}{2} & 0 \\ \nu & \nu & 0 & 1-\nu \end{bmatrix} \quad [7]$$

The incremental total strains, $\{\Delta\varepsilon\}$, in Eq. [5], are composed of elastic, $\{\Delta\varepsilon_e\}$, thermal, $\{\Delta\varepsilon_{th}\}$, inelastic strain, $\{\Delta\varepsilon_{in}\}$, and flow strain, $\{\Delta\varepsilon_{flow}\}$, components as given in Eq. [8].

$$\{\Delta\varepsilon\} = \{\Delta\varepsilon_e\} + \{\Delta\varepsilon_{th}\} + \{\Delta\varepsilon_{in}\} + \{\Delta\varepsilon_{flow}\} \quad [8]$$

Totals of all strains at a given time, $t+\Delta t$, are obtained by accumulating the strain increments at each prior time step. For example, the total strain is accumulated as follows, Eq. [9]:

$$\{\varepsilon^{t+\Delta t}\} = \{\varepsilon^{t}\} + \{\Delta\varepsilon^{t+\Delta t}\} \quad [9]$$

A. Thermal Strain

Thermal strains arise due to volume changes caused by both temperature differences and phase transformations, including solidification and solid-state phase changes between crystal structures, such as austenite and ferrite. The isotropic thermal strain vector, $\{\Delta\varepsilon_{th}\}$, given in Eq. [10], is based on the phase fractions and the thermal linear expansion function, TLE, discussed in Section X-C.

$$\{\Delta\varepsilon_{th}^{t+\Delta t}\} = \left(TLE(T^{t+\Delta t}) - TLE(T^{t})\right)\{1 \quad 1 \quad 0 \quad 1\}^T \quad [10]$$

B. Inelastic Strain

Inelastic strain includes both strain-rate independent plasticity and time dependent creep. Creep is significant at the high temperatures of this process and is indistinguishable from plastic strain. Thus, this work adopts a unified constitutive model of the mechanical behavior to capture the temperature- and strain-rate sensitivity of high temperature steel.

The inelastic strain rate, $\dot{\varepsilon}_{in}$, is described by different constitutive models according to microstructural state of the solid steel.

$$\dot{\bar{\varepsilon}}_{in} = \begin{cases} \dot{\bar{\varepsilon}}_{in-\delta} & ,\%\delta \geq 10\% \\ \dot{\bar{\varepsilon}}_{in-\gamma} & ,\%\delta < 10\% \end{cases} \quad [11]$$

$\dot{\bar{\varepsilon}}_{in-\delta}$ and $\dot{\bar{\varepsilon}}_{in-\gamma}$ are the equivalent inelastic strain rates of ferrite and austenite, respectively., as given below. The inelastic strain rate function follows the ferrite function, (δ or α), whenever the phase fraction of ferrite exceeds 10% of the total volume. This is justified by considering the steel with two phases to act as a composite material in which only a small amount of the weaker ferrite phase weakens the mechanical strength of the whole material. The plain carbon steels treated in this work are assumed to harden isotropically, so the von Mises loading surface, associated plasticity and normality hypothesis in the Prandtl-Reuss flow law is applied: [45]

$$\dot{\underset{\sim}{\varepsilon}}_{in} = \frac{3}{2}\dot{\bar{\varepsilon}}_{in}\frac{\underset{\sim}{\sigma}'}{\bar{\sigma}} \quad [12]$$

where $\underset{\sim}{\dot{\varepsilon}}_{in}$, $\underset{\sim}{\sigma}'$, $\bar{\sigma}$ and $\dot{\bar{\varepsilon}}_{in}$ are the plastic strain rate tensor, the deviatoric stress tensor, the equivalent stress scalar (or von-Mises effective stress), and equivalent inelastic strain-rate scalar, respectively. The ":" operator means standard term by term tensor multiplication. In this work, the equivalent inelastic strain rate, $\dot{\bar{\varepsilon}}_{in}$, bears a sign determined by the direction of the maximum principle inelastic strain, as defined in Eq. [13] in order to achieve kinematic behavior (Bauschinger effect) during reverse loading.

$$\dot{\bar{\varepsilon}}_{in} = c\sqrt{\frac{2}{3}\underset{\sim}{\dot{\varepsilon}}_{in} : \underset{\sim}{\dot{\varepsilon}}_{in}} \quad where \quad c = \begin{cases} \dfrac{\varepsilon_{\max}}{|\varepsilon_{\max}|} & \varepsilon_{\max} \geq \varepsilon_{\min} \\ \dfrac{\varepsilon_{\min}}{|\varepsilon_{\min}|} & \varepsilon_{\max} < \varepsilon_{\min} \end{cases} \tag{13}$$
$$where \quad \varepsilon_{\max} = \max(\varepsilon_{in11}, \varepsilon_{in22}, \varepsilon_{in33}) \quad \varepsilon_{\min} = \min(\varepsilon_{in11}, \varepsilon_{in22}, \varepsilon_{in33})$$

Eqs. [12] and [13] allow an isotropic scalar to represent the 3-D strain-rate state. Appendix B defines $\underset{\sim}{\sigma}'$, $\bar{\sigma}$, and Eq. [12] in 2-D generalized plane strain form. Parameter c (+1 or -1) makes the equivalent inelastic strain rate have the same sign as the maximum principle inelastic strain. The functions for the inelastic strain rate scalars, $\dot{\bar{\varepsilon}}_{in}$, described in Section X-D, must be integrated to find $\{\Delta\varepsilon_{in}\}$ needed in Eq. [8], as described previously in this Section.

C. Strain in Liquid Elements

In this model, the liquid elements are generally given no special treatment regarding material properties and finite element assembly. However, liquid reacts very differently from solid under external loads. It deforms elastically under hydrostatic force like a solid but deforms dramatically under shear force. If any liquid is present in a given finite element, a constitutive equation is used to generate an extremely rapid creep (shear) rate:

$$\dot{\bar{\varepsilon}}_{flow} = \begin{cases} cA\left(|c\bar{\sigma}| - \sigma_{yield}\right) & |c\bar{\sigma}| > \sigma_{yield} \\ 0 & |c\bar{\sigma}| \leq \sigma_{yield} \end{cases} \tag{14}$$

The parameter A is chosen to be 1.5×10^{8} MPa^{-1}s^{-1} to match the viscosity of molten steel [46]. Eq. [14] is another format of the linear viscous equation [43] of the laminar fluid which is a reasonable assumption for the liquid steel in the mushy zone. Liquid deforms under any nonzero shear stress according to Newtonian fluid dynamics. Thus, σ_{yield} should be zero. To avoid numerical difficulty, however, σ_{yield} is treated as a tolerance accuracy parameter with no physical nature and is given a value of 0.01 *MPa*.

This method effectively increases shear strain, and thus enforces negligible liquid strength and shear stress. The critical temperature where the liquid fraction is sufficient to make the element act as a liquid is the "coherency temperature", $T_{coherency}$, currently defined equal to the solidus temperature. To generalize this scalar strain rate to a multi-dimensional strain vector, the same Prandtl-Reuss Eqs. [12] and [13] are used as for the solid, $\dot{\bar{\varepsilon}}_{in}$.

This fixed-grid approach avoids the difficulties of adaptive meshing while allowing strain to accumulate in the mushy region. As in the real continuous casting process, the total mass of the liquid domain is not constant. The inelastic strain accumulated in the liquid represents mass transport due to fluid flow, so is denoted "flow strain". Positive flow strain indicates fluid feeding into the region. This is important for the prediction of hot tear cracks. The disadvantage of using this high creep rate function to model liquid is increasing the computational difficulty at the solidification front. This requires the use of a very robust local iteration algorithm [3].

V. FINITE ELEMENT IMPLEMENTATION

A. Heat Transfer and Solidification Model

The 3-node triangle finite element was employed to approximate temperature in the domain as a piece-wise linear function. The standard Galerkin method [44] applied to Eq. [2] gives the following global matrix equations.

$$[K]\{T\}+[C]\{\dot{T}\}=\{F_q\}+\{F_{qsup}\} \qquad [15]$$

$[K]$ is the conductance matrix including the effect of conductivity *k(T)*, and $[C]$ is the capacitance matrix including the effect of specific heat and latent heat in *H(T)*. Within each element, an effective specific heat c_{pe} is evaluated using a spatial averaging technique suggested by Lemmon [47].

$$c_{pe}=\frac{\partial H}{\partial T}=\sqrt{\frac{\left(\frac{\partial H}{\partial x}\right)^2+\left(\frac{\partial H}{\partial y}\right)^2}{\left(\frac{\partial T}{\partial x}\right)^2+\left(\frac{\partial T}{\partial y}\right)^2}} \qquad [16]$$

The [K] and [C] matrices are found from their element matrices, given in Appendix A, through standard FEM summation over the domain. A three-level time-stepping method proposed by Dupont [48] was adopted to solve Eq. [15]. Temperatures at the current time $t+\Delta t$ are found from the temperatures at the previous two time steps, t and $t-\Delta t$.

$$\{T\}=\frac{1}{4}\left\{3T^{t+\Delta t}+T^{t-\Delta t}\right\} \qquad [17]$$

$$\{\dot{T}\}=\left\{\frac{T^{t+\Delta t}-T^{t}}{\Delta t}\right\} \qquad [18]$$

Substituting Eqs. [17] and [18] into Eq. [15] and rearranging gives a recursive global matrix equation expressing the time and spatial discretization of the heat conduction equation, Eq. [2].

$$\left[\frac{3}{4}[K]+\frac{[C]}{\Delta t}\right]\left\{T^{t+\Delta t}\right\}=\{F_q\}+\{F_{qsup}\}-\frac{1}{4}[K]\left\{T^{t-\Delta t}\right\}+\frac{[C]}{\Delta t}\left\{T^{t}\right\} \qquad [19]$$

Eq. [19] is solved at each time step for the unknown nodal temperatures $\{T^{t+\Delta t}\}$ using a Choleski decomposition solver.[49] $\{F_q\}$, and $\{F_{qsup}\}$ are the heat flow load vectors containing the distributed heat flux at the domain boundary and the super heat flux at the internal moving boundary, respectively. On each domain boundary where heat flux is applied, the contributions from each element on the boundary are summed as follows:

$$\left\{F_q\right\} = \sum_{boundary \quad elements} \int [N]^T q \, dL = \sum_{boundary \quad elements} \begin{Bmatrix} \dfrac{q_{ij} L_{ij}}{2} \\ \dfrac{q_{ij} L_{ij}}{2} \end{Bmatrix} \quad [20]$$

where L_{ij} is the distance between node i and j. The heat flux function, q, is specified, such as equal to q_{gap} given in Section VII. $\left\{F_{qsup}\right\}$ is calculated similarly with a different set of boundary elements, using q_{sup} in Section VII.

B. Stress Model

Applying the standard Galerkin method to Eqs. [4] ~ [7] gives the following set of linear equations over the finite element domain,

$$\left[K\right]\left\{\Delta u\right\}^{t+\Delta t} = \left\{\Delta F_{th}\right\}^{t+\Delta t} + \left\{\Delta F_{in}\right\}^{t+\Delta t} + \left\{F_{fp}\right\}^{t+\Delta t} - \left\{F_{el}\right\}^{t} \quad [21]$$

where $[K]$, $\left\{\Delta F_{th}\right\}$, $\left\{\Delta F_{in}\right\}$, $\left\{F_{fp}\right\}$, and $\left\{F_{el}\right\}$ are the stiffness matrix and incremental force vectors due to incremental thermal strain, inelastic strain, ferrostatic pressure and external surface tractions at specified boundaries, and elastic strain corrections from the previous time step, respectively. Refer to Eqs. [64] - [67] in Appendix B for more details. At each time step, Eq. [21] is solved for the incremental displacements, $\left\{\Delta u\right\}$, using the Choleski method [49] and the total displacements are updated via Eq. [22].

$$\left\{u\right\}^{t+\Delta t} = \left\{u\right\}^{t} + \left\{\Delta u\right\} \quad [22]$$

Then, the total strains and stresses are updated from Eqs. [5] and [6], respectively. The six-node quadratic-displacement triangle elements use the same grid of nodes that were connected into three-node elements for the heat flow calculation. Further details are given in Appendix B.

VI. INTEGRATION OF THE CONSTITUTIVE MODEL

Highly strain-rate-dependent inelastic models require a robust numerical integration technique to avoid numerical difficulties. The non-linear equations to be integrated are given in Eqs. [23] and [24] by combining Eqs. [6] - [8], neglecting the second term on the right hand side of Eq. [6].

$$\underset{\approx}{\sigma}^{t+\Delta t} = \underset{\approx}{D}^{t+\Delta t} : \left(\underset{\approx}{\varepsilon}^{t} - \underset{\approx}{\varepsilon}_{th}^{t} - \underset{\approx}{\varepsilon}_{in}^{t} + \Delta\underset{\approx}{\varepsilon}^{t+\Delta t} - \Delta\underset{\approx}{\varepsilon}_{th}^{t+\Delta t} - \Delta\underset{\approx}{\varepsilon}_{in}^{t+\Delta t} \right) \quad [23]$$

$$\bar{\varepsilon}_{in}^{t+\Delta t} = \bar{\varepsilon}_{in}^{t} + \Delta\bar{\varepsilon}_{in}^{t+\Delta t} \quad [24]$$

The incremental equivalent plastic strain accumulated over a time step is given in Eq. [25] based on a highly nonlinear constitutive function, which depends on $\bar{\sigma}$ and $\bar{\varepsilon}_{in}$, which change greatly over the time step.

$$\Delta\bar{\varepsilon}_{in}^{t+\Delta t} = F\left(T, \bar{\sigma}^{t+\Delta t}, \bar{\varepsilon}_{in}^{t+\Delta t}, \%C\right)\Delta t \quad [25]$$

F is one of the constitutive functions given in Eqs. [46], [47] or [14] depending on the current material state. Substituting Eqs. [12] and [25] into Eqs. [23] and [24] and using fully implicit time stepping method, a new set of evolution equations are obtained as:

$$\underset{\approx}{\sigma}^{t+\Delta t} = \underset{\approx}{D}^{t+\Delta t} : \left(\underset{\approx}{\varepsilon}^{t} - \underset{\approx}{\varepsilon}_{th}^{t} - \underset{\approx}{\varepsilon}_{in}^{t} + \Delta \hat{\underset{\approx}{\varepsilon}} - \dot{\underset{\approx}{\varepsilon}}_{th}^{t+\Delta t} \Delta t - \frac{3}{2} F\left(T, \bar{\sigma}^{t+\Delta t}, \bar{\varepsilon}_{in}^{t+\Delta t}, \%C\right) \frac{\underset{\approx}{\sigma}^{t+\Delta t\,\prime}}{\bar{\sigma}^{t+\Delta t}} \Delta t \right) \qquad [26]$$

$$\bar{\varepsilon}_{in}^{t+\Delta t} = \bar{\varepsilon}_{in}^{t} + F\left(T, \bar{\sigma}^{t+\Delta t}, \bar{\varepsilon}_{in}^{t+\Delta t}, \%C\right) \Delta t \qquad [27]$$

Two tensors, $\underset{\approx}{\sigma}^{t+\Delta t}$ and $\Delta \hat{\underset{\approx}{\varepsilon}}$, and one scalar, $\bar{\varepsilon}_{in}^{t+\Delta t}$, comprise 13 unknown scalar fields for 3-D problems or 9 unknowns for the 2-D problem here, which require the solution of Eqs. [26] and [27]. Zhu implemented an alternating implicit-explicit mixed time integration scheme, which is based on an operator-splitting technique that alternates between local and global forms of the total strain increment and inelastic strain rate over each pair of successive steps [3]. Within each time step, $\underset{\approx}{\sigma}^{t+\Delta t}$ and $\bar{\varepsilon}_{in}^{t+\Delta t}$ are first solved using a fully implicit time integration technique based on the current best estimation of the total strain increment $\Delta \hat{\underset{\approx}{\varepsilon}}$, which is taken from the previous time step $\Delta \underset{\approx}{\varepsilon}^{t}$. This is a "local step" because it is spatially uncoupled.

Then, the improved estimates of $\underset{\approx}{\sigma}^{t+\Delta t}$ and $\bar{\varepsilon}_{in}^{t+\Delta t}$ from the "local step" are used to solve for $\Delta \underset{\approx}{\varepsilon}$ by explicit finite element spatial integration through Eqs. [21] and [5]. This is a "global step" [3].

There is still a tensor unknown in Eq. [26], which makes even the local time integration step computationally challenging. Lush *et. al.* transformed this tensor equation into a scalar equation for isotropic materials with isotropic hardening [50].

$$\bar{\sigma}^{t+\Delta t} = \bar{\sigma}^{*t+\Delta t} - 3\mu^{t+\Delta t} F\left(T, \bar{\sigma}^{t+\Delta t}, \bar{\varepsilon}_{in}^{t+\Delta t}, \%C\right) \Delta t \qquad [28]$$

where $\bar{\sigma}^{*t+\Delta t}$ is the equivalent stress of the stress tensor, $\underset{\approx}{\sigma}^{*t+\Delta t}$, defined below.

$$\underset{\approx}{\sigma}^{*t+\Delta t} = \underset{\approx}{D}^{t+\Delta t} : \left(\underset{\approx}{\varepsilon}^{t} - \underset{\approx}{\varepsilon}_{th}^{t} - \underset{\approx}{\varepsilon}_{in}^{t} + \Delta \hat{\underset{\approx}{\varepsilon}} - \dot{\underset{\approx}{\varepsilon}}_{th}^{t+\Delta t} \Delta t \right) \qquad [29]$$

Eqs. [27] and [28] form a pair of nonlinear scalar equations to solve in the local step for estimates of the two unknowns $\bar{\varepsilon}_{in}^{t+\Delta t}$ and $\bar{\sigma}^{t+\Delta t}$.

Stress Model Numerical Integration Procedure

Implementing the general 3-D procedure described above for the 2-D generalized plane strain assumption, the integration procedure used in CON2D within each time step is summarized as follows:

1. Estimate $\{\Delta\hat{\varepsilon}\}$ based on $\{\Delta u\}$ from the previous time step: $\{\Delta\hat{\varepsilon}\} = [B]\{\Delta u\}^{t}$.
2. Calculate $\{\sigma^{*}\}^{t+\Delta t}$, $\bar{\sigma}^{*}$ and $\{\sigma^{*\prime}\}^{t+\Delta t}$, needed to define the direction of the stress vector.

$$\{\sigma^{*}\}^{t+\Delta t} = [D]^{t+\Delta t} \left(\{\varepsilon\}^{t} - \{\varepsilon_{th}\}^{t} - \{\varepsilon_{in}\}^{t} + \{\Delta\hat{\varepsilon}\} - \dot{\varepsilon}_{th}^{t+\Delta t} \Delta t \{1 \quad 1 \quad 0 \quad 1\}^{T} \right) \qquad [30]$$

3. Solve the following two ordinary differential equations simultaneously for $\bar{\varepsilon}_{in}^{t+\Delta t}$ and $\bar{\sigma}^{t+\Delta t}$ at each local Gauss point, using a fully implicit bounded Newton-Raphson integration method from Lush [50]. This method gives the best robustness and efficiency of several alternative approaches evaluated [3]. Function *F* is either Kozlowski model III for γ, Eq. [46], the power law for δ, Eq. [47], or flow strain for liquid phase Eq. [14].

$$\bar{\varepsilon}_{in}^{t+\Delta t} = \bar{\varepsilon}_{in}^{t} + F\left(T, \bar{\hat{\sigma}}^{t+\Delta t}, \bar{\varepsilon}_{in}^{t+\Delta t}, \%C\right)\Delta t$$
$$\bar{\hat{\sigma}}^{t+\Delta t} = \bar{\sigma}^{*t+\Delta t} - 3\mu^{t+\Delta t} F\left(T, \bar{\hat{\sigma}}^{t+\Delta t}, \bar{\varepsilon}_{in}^{t+\Delta t}, \%C\right)\Delta t \qquad [31]$$

4. Expand this scalar stress estimate into vector form[2]:

$$\left\{\hat{\sigma}\right\}^{t+\Delta t} = \bar{\hat{\sigma}}^{t+\Delta t} \frac{\left\{\sigma^{*}{}'\right\}^{t+\Delta t}}{\bar{\sigma}^{*t+\Delta t}} + \frac{1}{3}\sigma_{m}^{*t+\Delta t}\left\{\delta\right\}^{T} \qquad [32]$$

5. Calculate $\dot{\bar{\varepsilon}}_{in}^{t+\Delta t}$ from $\bar{\hat{\sigma}}^{t+\Delta t}$ and $\bar{\varepsilon}_{in}^{t+\Delta t}$ using the appropriate F for the local material phase.
6. Expand this scalar inelastic strain estimate into a vector $\left\{\dot{\varepsilon}_{in}\right\}^{t+\Delta t}$ with the same direction as $\left\{\hat{\sigma}'\right\}^{t+\Delta t}$ using Prandtl-Reuss Eq. [12]; Update $\left\{\varepsilon_{in}\right\}^{t+\Delta t} = \left\{\varepsilon_{in}\right\}^{t} + \left\{\dot{\varepsilon}_{in}\right\}^{t+\Delta t}\Delta t$ only for solidified elements.
7. Use classic FEM spatial integration (Appendix B) to solve Eq. [21] for $\left\{\Delta u\right\}^{t+\Delta t}$ based on $\left\{\dot{\varepsilon}_{in}\right\}^{t+\Delta t}$.
8. Finally, find $\left\{\Delta\varepsilon\right\}^{t+\Delta t}$ from $\left\{\Delta u\right\}^{t+\Delta t}$ and update $\left\{\varepsilon\right\}^{t+\Delta t}$ and $\left\{\sigma\right\}^{t+\Delta t}$.

Overall, this alternating implicit-explicit scheme with the bounded Newton-Raphson iteration gives the best robustness and efficiency of several alternative FEM time integration approaches evaluated [3].

VII. TREATMENT OF THE MOLD - SHELL INTERFACE

Heat transfer does not depend directly on the force equilibrium equation because the mechanical dissipation energy is negligible. The heat flow and stress models are fully coupled with each other, however, when the gap between mold and steel shell is taken into account. Shrinkage of the shell tends to increase the thermal resistance across the gap where the shell is strong enough to pull away from the mold wall. This leads to hot and weak spots on the shell. This interdependence of the gap size and the thermal resistance requires iteration between the heat transfer and stress models. As the gap size is unknown in prior, the heat resistance is also unknown. Thus, iterations within a time step are usually needed. Contact between the mold wall and shell surface is discussed in Section VIII-B.

A. Interface Heat Transfer

When the coupled heat transfer and thermal stress analysis is performed, the heat transfer boundary condition at the steel surface is described by a gap heat resistor model shown in Figure 2, with parameter values listed in Table I. Heat leaves the steel shell via conduction and radiation across the interfacial gap. It is then conducted across the thin copper mold, and extracted by cooling water flowing across the back of the mold tube. The temperature and the heat convection coefficient of the cooling water are input from the results of a preliminary computation using the CON1D model, described elsewhere [51]. The contact resistance adopted in this model is several orders of magnitude larger than the physical contact resistance [46] between flat steel and copper surface because it includes the influence of oscillation marks [51]. The gap thickness is calculated during each iteration from the shell surface displacement and the mold wall position, according to the local values of the mold taper and distortion, which are

---

[2] $\left\{\sigma^{*}{}'\right\}^{t+\Delta t} = \left\{\sigma^{*}\right\}^{t+\Delta t} - \frac{1}{3}\sigma_{m}^{*t+\Delta t}\left\{\delta\right\}^{T}$; $\sigma_{m}^{*t+\Delta t} = \sigma_{x}^{*t+\Delta t} + \sigma_{y}^{*t+\Delta t} + \sigma_{z}^{*t+\Delta t}$; $\left\{\delta\right\} = \left\{1 \quad 1 \quad 0 \quad 1\right\}$

described in the next section. Once the gap size is determined, the heat flux, q_{gap}, across the interfacial layer between the mold wall and steel surface is solved together with the mold hot face temperature, T_{mold}:

$$q_{gap} = -\frac{T_{shell} - T_{water}}{r_{gapmold}} \qquad [33]$$

where

$$r_{gapmold} = \frac{1}{h_{water}} + \frac{T_{mold}}{k_{mold}} + \frac{\dfrac{d_{gap}}{k_{gap}} + r_{contact}}{1 + h_{rad}\left(\dfrac{d_{gap}}{k_{gap}} + r_{contact}\right)}$$

$$h_{rad} = 5.67 \times 10^{-8}\,\overline{e}\,(T_{shell} + T_{mold})(T_{shell}^2 + T_{mold}^2)$$

$$\overline{e} = \frac{1}{1/\varepsilon_m + 1/\varepsilon_s + 1}$$

$$T_{mold} = \frac{5.67 \times 10^{-8}\,\overline{e}\,T_{shell}^4 + T_{shell}/r_{mold} + T_{water}/r_{gap}}{1/r_{mold} + 1/r_{gap}}$$

$$r_{mold} = \frac{d_{mold} h_{water} + k_{mold}}{h_{water} k_{mold}}$$

$$r_{gap} = \frac{d_{gap}}{k_{gap}} + r_{contact}$$

B. Gap Size Calculation

The gap thickness, d_{gap}, is estimated for each boundary node at the shell surface, based on gaps from the previous iteration, n:

$$\hat{d}_{gap}^{n+1} = \max\left(\left\{u(d_{gap}^{n})\right\} \cdot \hat{n} - d_{wall}^{t+\Delta t}, d_{gapmin}\right)$$
$$where \qquad [34]$$
$$d_{wall}^{t+\Delta t} = d_{taper}^{t+\Delta t} - d_{molddist}^{t+\Delta t}$$

where $\{u\}$, $\hat{n}$, d_{wall}, d_{taper}, $d_{molddist}$ and d_{gapmin} are the displacement vector at boundary nodes, unit normal vector to the mold wall surface, mold wall position, mold wall position change due to mold distortion, and the minimum gap thickness, respectively. A positive d_{gap}, indicates a real space between the mold and shell.

The minimum gap value is set as:

$$d_{gapmin} = r_{contact} k_{gap} \qquad [35]$$

It physically represents the effective oscillation mark depth at the shell surface. When the calculated gap size is less than this minimum gap size, then, the contact resistance, $r_{contact}$, dominates heat transfer between the shell surface and the mold wall. Gap size variation within the minimum gap size is assumed not to affect the thermal resistance, which accelerates convergence.

C. Thermal – Stress Coupling

The overall flow of CON2D is shown in Figure 3. Within each time step, the computation alternates between the heat transfer and stress models through the following fully-coupled procedure:

1. The temperature field is solved based on the current best estimation of gap size, from the previous time step with Eq. [34]. The initial gap size at the beginning of the simulation is simply zero around the strand perimeter as the liquid steel at the meniscus flows to match the mold contour.
2. The incremental thermal strain is evaluated from the temperature field at the current and previous time steps, Eq. [10]. The inelastic strain is estimated by integrating Eq. [31] following the procedure described in Section VI. The global matrix equation, Eq. [21], is solved for displacements, strains, and stresses using the standard finite element method.
3. The gap sizes for the next iteration are updated by:

$$d_{gap}^{n+1} = \beta \hat{d}_{gap}^{n+1} + (1-\beta) d_{gap}^{n} \qquad [36]$$

   where β is chosen to be 0.5.
4. Finally, step 1 ~ 3 are repeated until the gap size difference between two successive heat transfer and stress iterations, n and $n+1$, is small enough:

$$d_{diff} = \sqrt{\frac{\sum_{nb}\left(d_{gap}^{n+1} - d_{gap}^{n}\right)^2}{\sum_{nb}\left(d_{gap}^{n+1}\right)^2}} \qquad [37]$$

   where nb is the number of boundary nodes. When d_{diff} becomes smaller than the specified "gap tolerance", $d_{\min}$, the gap size is considered converged.

VIII. MOLDELING THE MOLD WALL

The mold wall affects the calculation in two ways: 1) altering the size of the interfacial gap and associated heat transfer between the mold and strand through its distorted shape; and 2) constraining the shell from bulging due to the internal ferrostatic pressure.

A. Mold Wall Shape

The mold wall is defined in CON2D as a function of distance below the meniscus. The shape of the mold varies from its dimensions at the meniscus due to mold taper and mold distortion. The mold is tapered to follow the shrinkage of the steel strand to prevent excessive gaps from forming between the mold wall and shell surface, as well as preventing bulging of the shell. Linear taper is defined by providing the percentage per meter as follows:

$$d_{taper} = \frac{\%Taper/m}{100}\frac{W}{2} v_c\, t \qquad [38]$$

where W, v_c and t are the mold width, casting speed and current time below the meniscus, respectively. As the modeled section of the steel strand moves down from the meniscus, the mold wall distorts away from the solidifying shell, and tapers towards it.

Mold distortion arises from two main sources, thermal expansion of the mold wall due to heating during operation, and mold wear due to friction between the mold and the strand. For the billet casting simulation presented here, mold distortion is considered to be simple thermal expansion as follows, ignoring residual distortion and mold wear.

$$d_{molddist} = \alpha_{mold} \frac{W}{2}\left(\bar{T} - \bar{T}_0\right) \quad [39]$$

where $\bar{T}$ is the average temperature through the mold wall thickness as a function of the distance below mold exit, $\bar{T}_0$ is the average mold wall temperature where the solid shell begins at the meniscus, α_{mold} is the thermal expansion coefficient of the copper mold tube, and W is section width.

Arbitrary complex mold shapes can be modeled by providing an external data file or function with mold wall positions at different distances below the meniscus, and even around the perimeter. For example, complex 3-D mold distortion profiles [52] were used for slab casting simulations with CON2D [2, 6].

B. Contact Algorithm for Shell Surface Constraint

The mold wall provides support to the solidifying shell before it reaches the mold exit. A proper mold wall constraint is needed to prevent the solidifying shell from penetrating the mold wall, while also allowing the shell to shrink freely. Because the exact contact area between the mold wall and the solidifying shell is not known a priori, an iterative solution procedure is needed.

Some early finite element models solved contact problems by the Lagrange multiplier approach, which introduces new unknowns to the system as well as numerical difficulties [53]. This work adopts a method developed and implemented by Moitra [2, 6] which is tailored to this particular casting problem domain. It solves the contact problem only approximately, but is easy to implement and is more stable. Iteration within a time step proceeds as follows.

At first, the shell is allowed to deform freely without mold constraint. Then, the intermediate shell surface is compared to the current mold wall position. A fraction of all penetrating nodes, identified by Eq. [40], are restrained back to the mold wall position by a standard penalty method, and the stress simulation is repeated.

$$\{u\} \cdot \hat{n} - d_{wall} < \quad -d_{pen} \quad [40]$$

where d_{pen} is the specified penetration tolerance. Iteration continues until no penetration occurs.

The nodes to be constrained are chosen by checking three scenarios:

1. In Figure 4(a), a portion of the shell surface with length L penetrates the mold, and the maximum penetration is found at the centerline of the strand face. Those shell boundary nodes in the half of this violated length nearest to the face center, L_c, are constrained in the next iteration.
2. In Figure 4(b), the center of the shell surface penetrates the mold but does not penetrate the most. Those violated nodes from the maximum penetration position to the face center are constrained in the next iteration.
3. In Figure 4(c), the center of the shell surface does not penetrate the mold. That half of the violated nodes closest to the face center are constrained in the next iteration.

Commercial software, such as ABAQUS, generally constrains violated nodes one by one until convergence is reached. The present method is believed to be more computationally efficient for the particular quarter mold and behavior of interest in this work. The friction between the shell and mold surface is ignored in this model. This would need to be added to consider phenomena such as transverse cracks due to excessive taper.

IX. SOLIDIFICATION FRONT TREATMENT

A. Superheat Flux

Superheat is the amount of heat stored in the liquid steel that needs to be extracted before it reaches the liquidus temperature. Superheat is treated in one of two ways: 1) Heat conduction method and 2) Superheat flux method. The heat conduction method simply sets the initial steel temperature to the pouring temperature, and increases the conductivity of the liquid by 6.5 times to crudely approximate the effects of fluid flow. This method equally distributes the superheat over the solidification front. In reality, the superheat distribution is uneven due to the flow pattern in the liquid pool.

The second method first obtains the superheat flux distribution from a separate fluid flow computation, such as done previously for billets [54]. or slabs [55]. This superheat flux at a given location on the strand perimeter is applied to appropriate nodes on the solidification front. Specifically, it is applied to the two nodes just below the liquidus in those 3-node elements with exactly one node above the liquidus. This is shown in Figure 5, where the isotherm is the liquidus. The initial liquid temperature is set just above the liquidus, to avoid accounting for the superheat twice.

B. Ferrostatic Pressure

Ferrostatic pressure greatly affects gap formation by encouraging contact between the shell and mold, depending on the shell strength. The ferrostatic pressure is calculated by:

$$F_p = \rho g z \qquad [41]$$

where z is distance of the current slice from the meniscus found from the casting speed and the current time. Ferrostatic pressure is treated as an internal load that pushes the shell toward the mold wall, as shown in Figure 5. It is applied equally to those two nodes just below the coherency temperature that belong to those 3-node elements having exactly one of its 3 nodes above the $T_{coherency}$ isotherm. It is assembled to the global force vector through Eq. [64] in Appendix B, which gives:

$$\left\{F_{fp}\right\} = \sum_{moving\ \ boundary\ \ elements} \begin{Bmatrix} \dfrac{F_p L_{ij}}{2} \\ \dfrac{F_p L_{ij}}{2} \end{Bmatrix} \qquad [42]$$

where L_{ij} is the boundary length between node i and j within a 3-node element.

X. MATERIAL PROPERTIES

This work adopts temperature-dependent steel properties chosen to be as realistic as possible.

A. Phase Fraction Model

A pseudo-binary phase diagram for certain plain carbon steels [3] developed from measurements by WON [56] is incorporated to produce realistic phase fraction evolution

[3] Other compositions besides carbon are: 1.52%Mn, 0.015%S, 0.012%P, 0.34%Si

between the solidus and liquidus temperatures. Figure 6 shows the non-equilibrium Fe-C phase diagram, which defines the volume fractions of liquid, δ-ferrite and austenite used in this work. The classical lever rule is used to calculate phase fractions in each two-phase region and the lever rule for ternary systems is used in the three phase region [57]. The 100% and 75% solid lines are compared with ZST and ZDT measurements by Schmidtmann *et. al.* [38]. They match very well.

Figure 7 shows the phase fractions thus generated as a function of temperature for the 0.04%C carbon steel, which is used in Section XIII. Note that the liquid fraction decreases parabolically as the steel cools from its liquidus. This agrees with a more sophisticated micro-segregation model [38].

B. Thermal Properties

The temperature dependent conductivity function for plain carbon steel is fitted from measured data compiled by K. Harste [58] and is given in Eq. [43]. Figure 8 shows the conductivity for several typical plain carbon steels. The conductivity increases linearly through the mushy zone to the liquid by a factor of 6.5 to partly account for the effect of convection due to flow in the liquid steel pool [55].

$$\begin{aligned}
&K(W/mK) = K_\alpha f_\alpha + K_\delta f_\delta + K_\gamma f_\gamma + K_l f_l \\
&where \\
&K_\alpha = [80.91 - 9.9269\times10^{-2} T(^oC) + 4.613\times10^{-5} T(^oC)^2][1 - a_1(\%C)^{a_2}] \\
&K_\delta = [20.14 - 9.313\times10^{-3} T(^oC)][1 - a_1(\%C)^{a_2}] \\
&K_\gamma = 21.6 - 8.35\times10^{-3} T(^oC) \\
&K_l = 39.0 \\
&a_1 = 0.425 - 4.385\times10^{-4} T(^oC) \quad a_2 = 0.209 + 1.09\times10^{-3} T(^oC)
\end{aligned} \qquad [43]$$

The enthalpy curve used to relate heat content and temperature in this work, $H(T)$, is obtained by integrating the specific heat curve fitted from measured data complied by K. Harste [58] as given in Eq. [44]. Figure 9 shows the enthalpy for typical plain carbon steels.

$$H(J/Kg) = H_\alpha f_\alpha + H_\delta f_\delta + H_\gamma f_\gamma + H_l f_l$$

where

$$H_\alpha = \begin{cases} 5187583.4T(K)^{-1} - 85766.26 + 504.8146T(K) \\ -0.065555695T(K)^2 + 1.495553\times10^{-4}T(K)^3 & T(K) \le 800 \\ -1.109483\times10^9 T(K)^{-1} - 4720.324T(K) \\ +2.291682T(K)^2 + 4055624.6 & 800 < T(K) \le 1000 \\ -11501.07T(K) + 6.238181T(K)^2 \\ +5780384 & 1000 < T(K) \le 1042 \\ 34871.21T(K) - 16.01329T(K)^2 \\ -1.8379674\times10^7 & 1042 < T(K) \le 1060 \\ -10068.18T(K) + 2.99343T(K)^2 \\ -5.217657\times10^9 T(K)^{-1} + 1.282244\times10^7 & 1060 < T(K) \le 1184 \end{cases}$$

$$H_\delta = a_\delta[441.3942T(K) + 8.872118\times10^{-2}T(K)^2 + 50882.26]$$

$$where \quad a_\delta = \left[18125(\%C) + 1.96612\times10^6(\%C)^2\right]\left[43.839(\%C) + 1201.1\right]^{-1}$$

$$H_\gamma = a_\gamma[429.8495T(K) + 7.48901\times10^{-2}T(K)^2 + 93453.72] \qquad [44]$$

$$where \quad a_\gamma = \left[36601(\%C) + 1.90793\times10^6(\%C)^2\right]\left[43.839(\%C) + 1201.1\right]^{-1}$$

$$H_l = 824.6157\ T(K) - 104642.3$$

For the multi-phase region, both conductivity and enthalpy are calculated by weighted averaging their different phase fractions, *f*. The subscripts (α, δ, γ, and l) in Eqs. [43] and [44] represent α-ferrite, δ-ferrite, austenite and liquid, respectively. Density is assumed constant ($7400\,Kg/m^3$) in order to maintain constant mass.

C. Thermal Linear Expansion

The thermal linear expansion function is obtained from solid phase density measurements compiled by K. Harste [58] and Jablonka [59] and liquid density measurements by Jimbo and Cramb [60].

$$TLE = \sqrt[3]{\frac{\rho(T_0)}{\rho(T)}} - 1$$

where

$$\rho(Kg/m^3) = \rho_\alpha f_\alpha + \rho_\delta f_\delta + \rho_\gamma f_\gamma + \rho_l f_l$$

$$\rho_\alpha = 7880.76 - 0.3244T(^oC) - 2.7461\times10^{-5}T(^oC)^2 \qquad [45]$$

$$\rho_\delta = \frac{100[8010.71 - 0.4724T(^oC)]}{[100-(\%C)][1+13.43\times10^{-3}(\%C)]^3}$$

$$\rho_\gamma = \frac{100[8105.91 - 0.5091T(^oC)]}{[100-(\%C)][1+8.317\times10^{-3}(\%C)]^3}$$

$$\rho_l = 7100 - 73.2(\%C) - 0.1[8.28 - 0.874(\%C)][T(^oC) - 1550]$$

A simple mixture rule is applied to obtain the overall density from the values of different phases. Figure 10 shows the thermal linear expansion curves for the typical plain carbon steels.

D. Inelastic Constitutive Properties

The unified constitutive model developed here uses the instantaneous equivalent inelastic strain rate, $\dot{\bar{\varepsilon}}_{in}$, as the scalar state function, which depends on the current equivalent stress, $\bar{\sigma}$, temperature, T, the steel carbon content, and the current equivalent inelastic strain, $\bar{\varepsilon}_{in}$, which accumulates below the solidus temperature [61-63]. The model was developed to match tensile test measurements of Wray [62] and creep test data of Suzuki [64]. Model III by Kozlowski given in Eq. [46] is adopted to simulate the mechanical behavior of austenite.

$$
\begin{aligned}
&\dot{\bar{\varepsilon}}_{in-\gamma}\left(1/\sec.\right) = f_{\%C}\left[F_\gamma\right]^{f_3-1} F_\gamma \exp\left(-\frac{4.465\times10^{4o}K}{T\left({}^oK\right)}\right) \\
&where \\
&F_\gamma = c\bar{\sigma}\left(MPa\right) - f_1\bar{\varepsilon}_{in}\left|\bar{\varepsilon}_{in}\right|^{f_2-1} \\
&f_1 = 130.5 - 5.128\times10^{-3}T\left({}^oK\right) \\
&f_2 = -0.6289 + 1.114\times10^{-3}T\left({}^oK\right) \\
&f_3 = 8.132 - 1.54\times10^{-3}T\left({}^oK\right) \\
&f_{\%C} = 4.655\times10^4 + 7.14\times10^4\%C + 1.2\times10^5\left(\%C\right)^2
\end{aligned}
\tag{46}
$$

where the direction of $\bar{\sigma}$, c, is given in Eq. [13], except using the principal stresses instead of principle strain components.

A power law model was developed to model the behavior of δ-ferrite [11], given as follows:

$$
\begin{aligned}
&\dot{\bar{\varepsilon}}_{in-\delta}\left(1/\sec.\right) = 0.1F_\delta\left|F_\delta\right|^{n-1} \\
&where \\
&F_\delta = \frac{c\bar{\sigma}\left(MPa\right)}{f_C\left(T\left({}^oK\right)/300\right)^{-5.52}\left(1+1000\left|\bar{\varepsilon}_{in}\right|\right)^m} \\
&f_C = 1.3678\times10^4\left(\%C\right)^{-5.56\times10^{-2}} \\
&m = -9.4156\times10^{-5}T\left({}^oK\right) + 0.349501 \\
&n = \left(1.617\times10^{-4}T\left({}^oK\right) - 0.06166\right)^{-1}
\end{aligned}
\tag{47}
$$

Figure 11 compares the stresses measured by Wray [62] to those predicted by the constitutive models at 5% strain, integrated under different constant strain rates. The constitutive models give acceptable performance. This figure also shows that δ-ferrite, which forms at higher temperatures found near the solidification front, is much weaker than austenite. This greatly affects the mechanical behavior of the solidifying steel shell.

A simple mixture rule is not appropriate in two-phase regions that contain interconnecting regions of a much weaker phase. Thus, the constitutive model given in Eq. [47] is applied in the solid whenever the volume fraction of ferrite (δ-ferrite above 1400°C, α-ferrite below 900°C) is more than 10%. Otherwise, Eq. [46] is adopted.

To make the constitutive model properly handle kinematic hardening during reverse loading, the equivalent stress/strain used in Eqs. [46] and [47] are given the same sign as the principle stress/strain having the maximum magnitude. The inelastic strain rate, as a consequence, also bears a sign.

Two uniaxial tensile experiments [42, 63] and a creep experiment [64] on plain carbon steel at elevated temperatures were simulated by CON2D to test the performance of its constitutive models. Figures 12(a) and 12(b) show CON2D predictions of tensile test behavior of austenite and delta-ferrite at constant strain rate around 10^{-4} s^{-1} which is typically encountered in the shell during continuous casting [63]. The results also compare reasonably with experiments at small strain (< 5%), although they over-predict the stress when the strain exceeds 5%. Because the strain generally stays within 5% for the entire continuous casting process, the constitutive models are quite reasonable for this purpose. Figure 13(a) shows the CON2D predictions of creep test behavior at constant load. The inelastic strain predictions match the measurements reasonably well, especially at times shorter than 50s, of most concern to continuous casting in the mold region. Beyond this time, CON2D underpredicts creep, which is consistent with the overprediction of stress, observed in the tensile test cases. Monotonic loading is unlikely beyond this length of time, anyway. Figure 13(b) compares CON2D predictions and creep test measurements [64] under a sinusoidal alternating load with full reversal (R-ratio = 1.167). Although more measurements and computations of complex loading conditions would be helpful, these comparisons show that the constitutive models in CON2D are reasonable, even for conditions that include reverse loading.

E. Elastic Properties

The temperature-dependent elastic modulus curve used in this model is a stepwise linear fit of measurements by Mizukami *et. al.* [65] given in Figure 14. Unlike in some other models, the elastic modulus of the liquid here was given the physically realistic value of 10GPa. Poisson ratio is 0.3 constant. Measurements of higher Poisson ratios at high temperature are attributed to creep occurring during the experiment. Incorrectly incorporating part of the volume conserved plastic behavior, where $\upsilon = 0.5$, into the elastic υ will cause numerical difficulty for the solver.

XI. NUMERICAL PERFORMANCE

A 2-D transient elastic-visco-plastic thermal stress simulation with solidification, internal pressure, and contact is a challenging problem even for a super-computer. The efficient algorithms in CON2D allow the complete solution of practical problems in reasonable times with reasonable accuracy. Coupling between the thermal and stress models can cause instability, however, unless parameters, such as time step size, tolerances of gap size and penetration, are carefully chosen. Current experience indicates the initial time step for a fully coupled simulation with mold wall constraint should be 0.0001 sec., which is 10 times smaller than the smallest time step size adopted for uncoupled thermal stress simulation by Zhu [3]. The time step size can be increased 20-fold up to 0.005 sec. as the simulation progresses. Increasing time step size further does not speed up the simulation due to the need for more in-step iterations. It takes about 72 hours to perform a complete fully-coupled 19-s mold simulation of a 120mm$\times$120mm billet with 7381 nodes on a Pentium IV 1.7 GHz workstation running Windows 2000 Professional OS using less than 500 MB of RAM. The corresponding simulation without coupling allows larger time steps (0.001 – 0.5s) and takes only about 5 hours. Below-mold simulations allow even larger steps and take only about 1 hour [66].

Reasonable tolerances should be specified to achieve satisfactory gap size convergence while avoiding excessive mold wall penetration. The minimum gap, d_{gapmin}, is chosen here to be 0.012 mm, which is less than the effective thickness of the oscillation marks and surface roughness. Gaps smaller than this are considered to be converged. Thus, the effective oscillation mark depth dominates the heat resistance across the gap, and must be determined either by measurement or calibration. The tolerance for the mold wall penetration, d_{pen}, is chosen to be 0.001 mm, which is on the order of the incremental displacement between two consecutive time steps. Too large a tolerance tends to make the simulation inaccurate, while too small a tolerance makes the program overreact to small penetrations and slows down the simulation. The best value of d_{pen} depends on the problem. Generally, a smaller value is needed when the simulation region of interest is closer to the meniscus.

XII. MODEL VALIDATION

An analytical solution of thermal stress model in an unconstrained solidifying plate, derived by Weiner and Boley [67] is used here as an ideal validation problem for solidification stress models. Constants for this validation problem were chosen here to approximate the conditions of interest in this work and are listed in Table II.

The material in this problem has elastic-perfect plastic behavior. The yield stress drops linearly with temperature from 20 MPa at 1000°C to 0 MPa at the solidus temperature 1494.35°C. For the current elastic-viscoplastic model, this constitutive relation was transformed into a computationally more challenging form, the highly nonlinear creep function of Eq. [14] with $A=1.5\times10^8$ and $\sigma_{yield}=0.01\ MPa$ in the liquid. A very narrow mushy region, 0.1°C, is used to approximate the single melting temperature assumed by Boley and Weiner. In addition to the generalized plane strain condition in the axial z-direction, a similar condition was imposed in the y-direction (parallel to the surface) by coupling the displacements of all nodes along the top surface of the slice domain as shown in Figure 1(c). The analytical solutions were computed with MATLAB [68].

Figures 15 and 16 show the temperature and the stress distributions across the solidifying shell at different solidification times using an optimized mesh and time step, similar to that adopted for the 2-D billet casting simulation. The mesh was graduated, increasing in size from 0.3mm at the left end to 2.0mm at right end and time step size increased from 0.001sec. at the beginning to 0.1sec. at the end.

Figures 17 and 18 show the relative average errors, given in Eq. [48] for the temperature and stress predictions, respectively.

$$\begin{aligned}
Error_T(\%) &= \frac{\sum_1^N \sqrt{\left(T_i^{CON2D} - T_i^{Analytical}\right)^2}}{N\left|T_{melt} - T_{cold}\right|}\times 100 \\
Error_\sigma(\%) &= \frac{\sum_1^N \sqrt{\left(\sigma_i^{CON2D} - \sigma_i^{Analytical}\right)^2}}{N\left|\sigma(T_{melt}) - \sigma(T_{cold})\right|}\times 100
\end{aligned} \quad [48]$$

Accuracy of the CON2D predictions increases if the mesh and time step are refined together. A fine uniform mesh of 0.1 mm, with small uniform time step of 0.001 sec., produces relative average errors within 1% for temperature and within 2% for stress. However, the computational cost is also high. Note that the inaccuracy is severe at early times of the simulation, especially for the stress predictions. This is because the solidified layer initially spans only a few elements. As the solid portion of the plate grows thicker, the mesh size and time step requirements become less critical. Thus, a non-uniform mesh with increasing time step size is better to satisfy both accuracy and efficiency. The optimal choice, used in Figures 15 and 16, gives a decent prediction with the relative average errors within 2% for temperature and 3% for stress. A similar mesh was adopted for the actual billet casting simulation. This demonstrates that the model is numerically consistent and has an acceptable mesh.

XIII. APPLICATION TO BILLET CASTING

CON2D was next applied to simulate a plant trial conducted at POSCO, Pohang works, South Korea [18], for a 120-mm square section billet of 0.04%C steel cast at 2.2 m/min, where measurements were available. The mold had a single linear taper of 0.785%/m. Details of the material and operation conditions are given in Tables III and IV, respectively. Two simulations were performed to predict the temperature, stress and deformation evolutions of the billet shell using the 2-D L-shaped domain (Figure 1(b)) and a slice domain through the centerline of the billet face (Figure 1(c)) similar to the Boley & Weiner analytical problem. The interfacial heat transfer constants for both simulations are given in Table I and were found with the help of a dedicated heat transfer code, CON1D [51].

The superheat flux profile was obtained from coupled computations of turbulent flow and heat transfer in a round billet caster by Khodadadi et al. [54] for the case of Grashof number ($Gr = gW^3\left(TLE(T_{pour}) - TLE(T_m)\right)/\nu^2$) is 1×10^8. This value is the closest case to the current problem conditions where the Grashof number is 2×10^7 and confirms that natural convection is unimportant in this process. The heat flux was calculated from the Nusselt number, *Nu*, and mean liquid temperature, T_m, results given as a function of distance below meniscus [54], using their values of liquid steel conductivity, $k = 29.8W/mK$, mold section size, *W=200mm* and 33 ^{o}C superheat, except for re-adjusting the superheat temperature difference as follows:

$$q_{\sup} = \frac{Nu\, k(T_m - T_{liq})}{W}\frac{\left(T_{pour} - T_{liq}\right)_{posco}}{\left(T_{pour} - T_{liq}\right)_{khod}} \qquad [49]$$

where T_{pour} and T_{liq} are the pouring and liquidus temperatures, respectively. The resulting superheat flux profile is shown in Figure 19. Note that the total heat integrated from Figure 19 over the mold surface, 48.6*kW*, matches the superheat for the current problem, $\left(T_{pour} - T_{liq}\right)\rho c_p v_c = 46kW$.

The heat flux and mold wall temperatures predicted by CON2D along the billet face center are shown in Figures 20 and 21 respectively. These results slightly underpredict the measurements of thermocouples embedded in the mold wall, which should lie almost exactly between the hot and cold face temperatures [69]. The total heat extracted by the mold, 128.5 *kW*, is 17% lower than the plant measurements based on a heat balance of the mold cooling water (8K temperature rise at 9.2m/s slot velocity) of 154*kW* [18]. This is consistent with underprediction of the mold temperatures.

The predicted shell growth for this CON2D simulation is given in Figure 22, as indicated by the evolution of the solidus and liquidus isotherms. This is compared with measurements of the solid-liquid interface location, obtained by suddenly adding FeS tracer into the liquid pool during steady-state casting [18]. Longitudinal and transverse sections through the billet were cut from the final product. The transverse section was 285 mm from the meniscus when the FeS tracer was added. Because FeS tracer cannot penetrate the solid steel shell, sulfur prints of sections cut through the fully-solidified billet reveal the location of the solidification front and shell thickness profile at a typical instant during the process [18]. The CON2D predictions match along the centerline beyond the first 80mm below the meniscus, where the shell remains in contact the mold, suggesting that the heat transfer parameters are reasonably accurate.

The shell surface position profile down the centerline is shown in Figure 23, together with the mold wall position, which includes both the taper, and the mold distortion profile calculated from the CON1D temperature results using Eq. [39] [51]. The shell surface generally follows the mold wall with no obvious penetration, validating the contact algorithm. Note, however, that a slight gap opens up within the first 25mm. Although this effect is believed to be physically reasonable owing to rapid initial shrinkage of the steel, it is exaggerated here, owing to numerical difficulties during the initial stages of solidification. This causes an overprediction of the drop in initial heat flux and temperature observed in Figure 20. This drop is followed by increased heat flux (and corresponding mold wall temperature) after full contact is re-established, which has also been observed in other measurements [70].

The simulation features a detailed prediction of temperature, shrinkage, and stress in the region of the rounded billet corner. The evolution of the increases in gap size and surface temperature are given in Figures 24 and 25 near (20mm) to the centerline of the billet face and at various locations, 0, 5, 10, and 15mm, from the billet corner. The corresponding large drops in heat flux are included in Figure 20. The solidifying shell quickly becomes strong enough to pull the billet corner away from the mold wall and form a gap around the corner region. The gap greatly decreases local heat flow in the corner, causing the mold wall temperature to drop.

The drop in mold temperature near the corner over the initial 80mm is more than expected in reality, because the simple mold model of CON2D in Eq. [33] neglects heat conduction around the corner and along the casting direction. Thus, these predictions are not presented. This latter effect, which is included in CON1D [51], also contributed to the convergence difficulties along the centerline discussed in Figure 23. Fortunately, it has little other effect on heat flux or shell behavior.

Figure 24 shows how a permanent gap forms after 40mm below the meniscus, which grows to over 0.3mm thick by half-way down the mold, growing little after that. Corresponding gaps form adjacent to the corner at later times, reaching smaller maxima part-way down the mold. These gaps form because the simple linear taper of the mold walls was insufficient to match shrinkage of the shell. The corner effect decreases with distance from the corner and disappears beyond 15mm from the corner.

The corner gap and drop in heat flux causes a hot spot at the corner region, as shown in the surface temperature profiles of Figure 25. CON2D predicts that the shell corner reheats slightly and reaches 150^{o}C hotter than the billet face center, for the conditions of this trial. The decreased heat flux also produces less solidification in the corner, as illustrated in Figure 26 at 285mm below the meniscus. The predicted shell thinning around the corner is consistent with the plant measurements from the sulfur print, as quantified in Figures 22 and 26. The predictions here are also consistent with those of Park *et. al.* , who modeled how increasing billet mold corner radius leads to more severe hot and thin spots near the corner [18]. This tends to validate the CON2D model and the simple constant interfacial heat transfer parameters used to produce these results. Improving the accuracy would likely require a more complex model of gap heat transfer that considered details of surface roughness, including differences between center and corner.

Figure 27 shows the evolution of surface stress components near the centerline of the billet face. Stress normal to the surface (x-direction) is effectively equal to zero, which indicates that the 0.785%/m mold taper never squeezes the billet. The stress components perpendicular to the solidification direction (y-direction tangential to surface and z-casting direction) are generally very similar, which matches the behavior expected from the analytical test solution [67]. These stresses grow slowly in tension during the period of increasing heat extraction rate from 20 to 100mm below the meniscus. They reach a maximum of almost 3 MPa due to the increase in shell strength at lower temperature that accompanies the transformation from δ-ferrite to austenite. This is shown in the through-thickness profile of these same stress components in Figure 28(a), but calculated with the 1-D slice domain. The surface tensile stress peak does not penetrate very deep, owing to the very thin layer of material colder than 10% delta-ferrite. Thus, this peak might cause very shallow fine surface cracks, but nothing deeper.

The surface stresses in Figure 27 suddenly turn compressive beyond 100mm due to the sudden change in heat extraction rate at this distance (see Figure 20). Surface compression arises because the subsurface begins to cool and shrink faster than the surface. This causes a corresponding increase in subsurface tension near the solidification front that might lead to subsurface cracks. The surface stays in compression from -4 to -6 MPa for the remaining time in the mold.

During the time beyond 100mm, the stress profile, Figure 28(b), is qualitatively similar to that of the analytical test problem, as expected. Differences arise from the variation in steel strength between the δ-ferrite and austenite. Stresses in the liquid, mushy zone and δ-ferrite are always very small. Tensile stress increases rapidly during the phase transformation, which takes place at the low end of the δ+γ region of Figure 28. When the δ-ferrite region is thin, this tensile stress is more likely to create strains significant to generate cracks. These results illustrate the widely accepted knowledge that surface cracks initiate near the meniscus, while subsurface cracks form lower down.

Figures 29(a) and (b) show the different components of strain (y-direction) through the shell thickness near the billet face center corresponding to the stresses in Figure 28. Thermal strains dominate in the solid and generate the other strains due to the constraint of adjacent layers of steel. Small elastic strains are generated by the mismatch of thermal strain, although the stresses they generate may still be significant. Inelastic strain is generated in regions of high-stress, starting in the δ+γ region. It is high at the surface at the top of the mold and later grows in the austenite. Note that inelastic strains are all tensile throughout the shell. The δ and mushy zones behave elastically with very low stresses. This is fortunate as these phases are very weak and cannot accommodate much inelastic strain before cracking. Flow strain in the liquid occurs to accommodate the total strain, which is naturally flat, owing to the constraint by the solid.

Figure 30 shows the "hoop" stress component (y direction parallel to billet surface and perpendicular to casting direction) at an off-corner location (10mm above the billet corner) through the shell thickness at 100mm, 500mm, and 700mm (mold exit) below meniscus. Stresses all behave similarly to the corresponding locations along the billet centerline, except that the tension and compression are lower. This is expected due to the slower cooling rates, shallower temperature gradients, and higher temperatures near the corner.

Figures 31 and 32 show contours of the stress and inelastic strain components perpendicular to the solidification direction superimposed on the distorted billet at mold exit with isotherms. The insufficient 0.785%/m taper of this mold is unable to support the billet which allows a slight bulge (0.25 mm at mold exit). Regions of high tensile stress and inelastic strain are indicated at the off-corner subsurface (10 ~ 20 mm from the corner and 2 ~ 6 mm beneath the surface).

XIV. CONCLUSIONS

A transient, two-dimensional, finite element model has been developed to quantify the temperature, stress and strain distributions in the solidifying shell in the continuous casting of steel. This is a Lagrangian approach in generalized plane strain that reasonably predicts the 3-D stress and strain state by solving energy and force balance equations within a 2-D transverse slice domain. Superheat dissipation and ferrostatic pressure are both taken account through internal boundary conditions. Unified elastic-viscoplastic constitutive models for both austenite and δ-ferrite phases of the steel match tensile and creep test data. Liquid is given physically reasonable properties including a high viscoplastic shear rate and small yield stress. A robust and efficient time integration technique, alternating local-global method, is adopted to integrate the highly non-linear constitutive equations. An efficient contact algorithm allows the model to properly treat shell surface interaction with the mold wall.

The model is validated by extensive comparisons with an analytical solution of thermal stress in an infinite solidifying plate, which justify the choice of mesh and time step size. The model is applied to simulate a 120-mm square billet continuously cast at 2.2m/min and the results compare favorably to in-plant measurements of thermocouples embedded in the mold walls, heat balance on the cooling water, and thickness of the solidified shell.

CON2D is a useful tool to gain quantitative understanding of issues pertaining to thermal mechanical behavior of the solidifying shell during the continuous casting of steel slabs and billets. It is being applied to investigate taper in billets [71] and slabs [72], minimum shell thickness to avoid breakouts [30], maximum casting speed to avoid longitudinal cracks due to off-corner bulging below the mold [66], and other phenomena.

ACKNOWLEDGEMENTS

The authors thank the steel industry members of the Continuous Casting Consortium at UIUC for their financial support of this project. Work by previous students, A. Moitra, H. Zhu, and J. Parkman, on the CON2D program is also gratefully acknowledged. The authors also thank the National Center for Supercomputing Applications (NCSA) for computational resources.

REFERENCES

1. W.R. Storkman: Optimization of Mold Taper Design Using Mathematical Models of Continuous Steel Slab Casting, Masters Thesis, University of Illinois, 1990.
2. A. Moitra: Thermo-Mechanical Model of Steel Shell Behavior in Continuous Slab Casting, Ph.D. Thesis Thesis, UIUC, 1993, p. 217.
3. H. Zhu: Coupled Thermal-Mechanical Finite-Element Model with Application to Initial Solidification, Ph.D. Thesis Thesis, UIUC, 1996, p. 132.
4. J.-C.T. Parkman: Simulation of Thermal Mechanical Behavior During Initial Solidification of Steel, Master Thesis Thesis, UIUC, 2000, p. 139.
5. W.R. Storkman and B.G. Thomas: "Mathematical Models of Continuous Slab Casting to Optimize Mold Taper", Modeling of Casting and Welding Processes, A.G. Giamei and G.J. Abbaschian, eds., (Palm Coast, FL), Engineering Foundation, 1988, vol. 4, pp. 287-97.
6. A. Moitra, B.G. Thomas and H. Zhu: "Application of a thermo-mechanical model for steel shell behavior in continuous slab casting", 76th Steelmaking Conference, ISS, ed., (Dallas, TX), Warrendale, PA, 1993, vol. 76, p. 657.
7. B.G. Thomas, A. Moitra and W.R. Storkman: "Optimizing Taper in Continuous Slab Casting Molds Using Mathematical Models", in Proceedings, 6th International Iron and Steel Congress, vol. 3, Iron & Steel Inst. Japan, Tokyo, 1990, pp. 348-55.
8. B.G. Thomas and H. Zhu: "Thermal Distortion of Solidifying Shell in Continuous Casting of Steel", in Proceedings of Internat. Symposia on Advanced Materials & Tech. for 21st Century, I. Ohnaka and D. Stefanescu, eds., TMS, Warrendale, PA, 1996, pp. 197-208.
9. G.D. Lawson, S.C. Sander, W.H. Emling, A. Moitra and B.G. Thomas: "Prevention of shell thinning breakouts associated widening width changes", 77th Steelmaking Conference, I.a.S. Society, ed., (Chicago, IL), Iron and Steel Society, Warrendale, PA, 1994, p. 239.
10. B.G. Thomas, A. Moitra and R. McDavid: "Simulation of Longitudinal Off-Corner Depressions in Continuously-Cast Steel Slabs", ISS Transactions, 1996, vol. 23 (4), pp. 57-70.
11. B.G. Thomas and J.T. Parkman: "Simulation of Thermal Mechanical Behaviour During Initial Solidification", Thermec '97 Intl. Conf. on Thermomechanical Proc. of Steel and Other Materials, TMS, ed., (Wollongong, Australia), TMS, Warrendale, PA, 1997, vol. II, pp. 2279-85.
12. B.G. Thomas and J.T. Parkman: "Simulation of Thermal Distortion of a Steel Droplet Solidifying on a Copper Chill", TMS Annual Meeting, M.C.a.E. Lavernia, ed., (San Antonio, TX), 1998.
13. A. Grill, J.K. Brimacombe and F. Weinberg: "Mathematical Analysis of Stresses in Continuous Casting of Steel", Ironmaking Steelmaking, 1976, vol. 3 (1), pp. 38-47.
14. K. Sorimachi and J.K. Brimacombe: "Improvements in Mathematical Modelling of Stresses in Continuous Casting of Steel", Ironmaking Steelmaking, 1977, vol. 4 (4), pp. 240-45.
15. J.O. Kristiansson: "Thermomechanical Behavior of the Solidifying Shell Within Continuous-Casting Billet Molds - A Numerical Approach", J. Thermal Stresses, 1984, vol. 7, pp. 209-26.
16. J.E. Kelly, K.P. Michalek, T.G. O'Connor, B.G. Thomas and J.A. Dantzig: "Initial Development of Thermal and Stress Fields in Continuously Cast Steel Billets", Metall. Trans. A, 1988, vol. 19A (10), pp. 2589-602.
17. J.R. Boehmer, G. Funk, M. Jordan and F.N. Fett: "Strategies for coupled analysis of thermal strain history during continuous solidification processes", Advances in Engineering Software, 1998, vol. 29 (7-9), pp. 679-97.

18. J.-k. Park, B.G. Thomas and I.V. Samarasekera: "Analysis of Thermo-Mechanical Behavior in Billet Casting with Different Mold Corner Radii", Ironmaking and Steelmaking, 2002, vol. 29 (5), pp. 359-75.
19. V.D. Fachinotti and A. Cardona: A fixed-mesh Eulerian-Lagrangian approach for stress analysis in continuous casting, Instituto Argentino de Siderurgia, Carlos della Paolera 226, Buenos Aires, 1001, Argentina, 2002, p.29, in press.
20. J.-E. Lee, T.-J. Yeo, K.H. Oh, J.-K. Yoon and U.-S. Yoon: "Prediction of Cracks in Continuously Cast Beam Blank through Fully Coupled Analysis of Fluid Flow, Heat Transfer and Deformation behavior of Solidifying Shell", Metall. Mater. Trans. A, 2000, vol. 31A (1), pp. 225 - 37.
21. K. Sorimachi and T. Emi: "Elastoplastic Stress Analysis of Bulging as a Major Cause of Internal Cracks in Continuously Cast Slabs", Tetsu-to-Hagane (J. Iron Steel Inst. Jpn.), 1977, vol. 63 (8), pp. 1297-304.
22. A. Grill and K. Schwerdtfeger: "Finite-element analysis of Bulging Produced by Creep in Continuously Cast Steel Slabs", Ironmaking Steelmaking, 1979, vol. 6 (3), pp. 131-35.
23. K. Kinoshita, T. Emi and M. Kasai: "Thermal Elasto-plastic Stress Analysis of Solidifying Shell in Continuous Casting Mold", Tetsu to Hagane, 1979, vol. 1979 (14), p. 2022.
24. F.G. Rammerstorfer, C. Jaquemar, D.F. Fischer and H. Wiesinger: "Temperature Fileds, Solidification Progress and Stress Development in the Strand During A Continuous Casting Process of Steel", in Numerical Methods in Thermal Problems, R.W. Lewis and K. Morgan, eds., Pineridge Press, 1979, pp. 712-22.
25. J.O. Kristiansson: "Thermal Stresses in the Early Stage of Solidification of Steel", J. Therm. Stresses, 1982, vol. 5 (3-4), pp. 315-30.
26. I. Ohnaka and Y. Yashima: "Stress Analysis of Steel Shell Solidifying in Continuous Casting Mold", Modeling and Control of Casting and Welding Processes. IV, (Palm Coast, Florida, USA), TMS/AIME, 420 Commonwealth Dr., Warrendale, Pennsylvania 15086, USA, 1988, pp. 385-94.
27. T.C. Tszeng and S. Kobayashi: "Stress analysis in solidification processes: Application to continuous casting", International Journal of Machine Tools and Manufacture [INT. J. MACH. TOOLS MANUF.], 1989, vol. 29 (1), pp. 121-40.
28. H. Zhu: Coupled Thermal-Mechanical Fixed-Grid Finite-Element Model with Application to Initial Solidification, PhD Thesis, University of Illinois, 1997.
29. J. Parkman: Simulation of Thermal-Mechanical Behavior During Initial Solidification of Steel, M.S. Thesis, University of Illinois, 2000.
30. C. Li and B.G. Thomas: "Analysis of the Potential Productivity of Continuous Cast Molds", Brimacombe Memorial Symposium, (Vancouver, Canada), Canadian Inst. Min. Metall., 2000, p. 17.
31. A.E. Huespe, A. Cardona and V. Fachinotti: "Thermomechanical model of a continuous casting process", Computer Methods in Appl. Mech. & Engr., 2000, vol. 182 (3), pp. 439-55.
32. A. Ramacciotti: "Thermo-mechanical Behaviour of the Solidified Shell in a "Funnel-shaped" Mold for Continuous Casting of Thin Slabs", Steel Research, 1988, vol. 59 (10), pp. 438-48.
33. T.G. O'Conner: Three-Dimensional Mathematical Modeling of the Thin Slab Continuous Casting Process, Ph.D. Thesis, University of Illinois, 1992.
34. J.-K. Park: Thermo-Mechanical Phenomena In High Speed Continuous Casting Processes, PhD Thesis, University of British Columbia, 2002.

35. B.G. Thomas: "Mathematical Modeling of the Continuous Slab Casting Mold : A State of the Art Review", in 74th Steelmaking Conf. Proc., vol. 74, ISS, Warrendale, PA, 1991, pp. 105-18.
36. B.G. Thomas: "Fundamentals of Continuous Casting: Modeling", in Making, Shaping and Treating of Steel: Continuous Casting, vol. 5, A. Cramb, ed., AISE Steel Foundation, Pittsburgh, PA, 2003, pp. pp. 5.1-5.24.
37. B.G. Thomas and L. Zhang: "Mathematical Modeling of Fluid Flow in Continuous Casting: a Review", ISIJ Internat., 2001, vol. 41 (10), pp. 1185-97.
38. Y.M. Won and B.G. Thomas: "Simple Model of Microsegregation during Solidification of Steels", Metallurgical and Materials Transactions A, 2001, vol. 32A (July, 2001), pp. 1755-67.
39. B.G. Thomas, G. Li, A. Moitra and D. Habing: "Analysis of Thermal and Mechanical Behavior of Copper Molds during Continuous Casting of Steel Slabs", Iron and Steelmaker (ISS Transactions), 1998, vol. 25 (10), pp. 125-43.
40. B.G. Thomas: "Modeling of the Continuous Casting of Steel: Past, Present, and Future, Dr. J. Keith Brimacombe Lecture", Metal. & Material Trans., 2002, vol. 33B (Dec.), pp. 795-812.
41. L. Yu: Bulging in Continuous Cast Steel Slabs, M.S. Thesis, University of Illinois, 2000.
42. Y. Won, T.-J. Yeo, D. Seol and K. Oh: "A New Criterion for Internal Crack Formation in Continuously Cast Steels", Metall. Trans. B, 2000, vol. 31B (4), p. 779~94.
43. J.A. Dantzig and C.L. Tucker: Modeling in Materials Processing, Cambridge University Press, 2001.
44. O.C. Zienkiewicz and R.L. Taylor: The Finite Element Method, 5th ed., vol. 1, Butterworth-Heinemann, Oxford ; Boston, 2000, p. 689.
45. J. Lemaitre and J.L. Chaboche: Mechanics of Solid Materials, Cambridge University Press, New York, NY, 1990, p. 556.
46. R.C. Weast: Handbook of Chemistry and Physics. 1971.
47. E. Lemmon: "Multi-dimentional Integral Phase Change Approximations for Finite-Element Conduction Codes", in Numerical Methods in Heat Transfer, vol. 1, R.W. Lewis, K. Morgan and O.C. Zienkiewicz, eds., John Wiley & Sons, 1981, pp. 201-13.
48. T. Dupont, G. Fairweather and J.P. Johnson: "Three-Level Galerkin Methods for Parabolic Equations", SIAM Journal on Numerical Analysis, 1974, vol. 11 (2), pp. 392-410.
49. G.E. Forsythe and C.B. Moler: Computer solution of linear algebraic systems, Prentice-Hall series in automatic computation, Prentice-Hall, Englewood Cliffs, N.J., 1967.
50. A.M. Lush, G. Weber and L. Anand: "An Implicit Time-Integration Procedure for a Set of Integral Variable Constitutive Equations for Isotropic Elasto-Viscoplasticity", International Journal of Plasticity, 1989, vol. 5, pp. 521-49.
51. Y. Meng and B.G. Thomas: Billet Casing Analysis by CON1D, Metal Processing and Simulation Lab, Mechanical & Industrial Engineering Department,University of Illinois at Urbana-Champaign, Report, 2001.
52. B.G. Thomas, G. Li, A. Moitra and D. Habing: "Analysis of Thermal and Mechanical Behavior of Copper Molds during Continuous Casting of Steel Slabs", in 80th Steelmaking Conf. Proc., vol. 80, ISS, Warrendale, PA, 1997, pp. 183-201.
53. B. Nour-Omid and P. Wriggers: "A Two Level Iteration Method for Solution of Contact Problems", Computer Methods in Applied Mechanics & Engineering, 1986, vol. 54, pp. 131-44.

54. J.M. Khodadadi, X.K. Lan and F. Shen: "Turbulent Mixed Convective Liquid Steel Flow and Heat Transfer in Continuous Casting Molds", The 28th National Heat Transfer Conference and Exhibition, (San Diego, CA), 1992, vol. 196, pp. 59-67.
55. X. Huang, B.G. Thomas and F.M. Najjar: "Modeling Superheat Removal During Continuous Casting of Steel Slabs", Metallurgical Transactions B, 1992, vol. 23B (3), pp. 339-56.
56. Y.M. Won, K.-h. Kim, T.-j. Yeo and K.H. Oh: "Effect of Cooling Rate on ZST, LIT and ZDT of Carbon Steels Near Melting Point", ISIJ International, 1998, vol. 38 (10), pp. 1093-99.
57. M.C. Flemings: Solidification Processing, McGraw-Hill Series in Materials Science and Engineering, M.B. Bever, M.E. Shank, C.A. Wert and R.F. Mehl, eds., McGraw-Hill, 1974, p. 364.
58. K. Harste: Investigation of the shrinkage and the origin of mechanical tension during the solidification and successive cooling of cylindrical bars of Fe-C alloys, Ph.D. Dissertation Thesis, Technical University of Clausthal, 1989, p. 115.
59. K. Harste, A. Jablonka and K. Schwerdtfeger: "Shrinkage and Formation of Mechanical Stresses During Solidification of Round Steel Strands", 4th International Conference Continuous Casting. Preprints. Vol. , ,, (Brussels, Belgium), Verlag Stahleisen, P.O. Box 8229, D-4000, Dusseldorf 1, FRG, 1988, vol. 2, pp. 633-44.
60. I. Jimbo and A. A. W. Cramb: "The Density of Liquid Iron--Carbon Alloys", Metallurgical Transactions B (USA), 1993, vol. 24B (1), pp. 5-10.
61. P. Kozlowski, B.G. Thomas, J. Azzi and H. Wang: "Simple Constitutive Equations for Steel at High Temperature", Metall. Trans. A, 1992, vol. 23A (3), pp. 903-18.
62. P.J. Wray: "Plastic Deformation of Delta-Ferritic Iron at Intermediate Strain Rates", Metall. Trans. A, 1976, vol. 7A (November), pp. 1621-27.
63. P.J. Wray: "Effect of Crabon Content on the Plastic Flow of Plain Carbon Steels at Elevated Temperatures", Metall. Trans. A, 1982, vol. 13A (January), pp. 125-34.
64. T. Suzuki, K.H. Tacke, K. Wunnenberg and K. Schwerdtfeger: "Creep Properties of Steel at Continuous Casting Temperatures", Ironmaking and Steelmaking, 1988, vol. 15 (2), pp. 90-100.
65. H. Mizukami, K. Murakami and Y. Miyashita: Tetsu-to-Hagane (J. Iron Steel Inst. Jpn.), 1977, vol. 63 (146), pp. S-652.
66. C. Li and B.G. Thomas: "Maximum Casting Speed for Continuous Cast Steel Billets Based on Sub-Mold Bulging Computation", in Steelmaking Conf. Proc., vol. 85, ISS, Warrendale, PA, 2002, pp. 109-30.
67. J.H. Weiner and B.A. Boley: "Elasto-Plastic Thermal Stresses in A Solidifying Body", J. Mech. Phys. Solids, 1963, vol. 11, pp. 145-54.
68. T. Mathworks Inc.: MATLAB User Manual, Ver. 5.3, Natick, MA 01760, 1999.
69. J.K. Park, C. Li, B.G. Thomas and I.V. Samarasekera: "Analysis of Thermo-Mechanical Behavior In Billet Casting", 60th Electric Furnace Conference, W. ISS, PA, 2001, ed., (San Antonio, TX), ISS, Warrendale, PA, 2001, 2002, vol. 60, p. 17.
70. C. Chow: The Effects of High Speed Casting on the Mould Heat Transfer, Billet Solidification, and Mould Taper Design of Continuously Cast Steel Billets, MS Thesis, University of British Columbia, 2001.
71. C. Li and B.G. Thomas: "Ideal Taper Prediction for Billet Casting", in Steelmaking Conf. Proc., vol. 86, ISS, Warrendale, PA, 2003,
72. C. Ojeda and B.G. Thomas: "Ideal Taper Prediction For Slab Casting", ISSTech 2003, W. ISS, PA, 2001, ed., (Indianapolis, IN), ISS, Warrendale, PA, 2001, 2003.

73. R.D. Cook, D.S. Malkus and M.E. Plesha: Concepts and Applications of Finite Element Analysis, 3rd ed., John Wiley & Sons, New York, 1989, p. 630.
74. T.W. Clyne, M. Wolf and W. Kurz: "The Effect of Melt Composition on Solidification Cracking of Steel, with Particular Reference to Continuous Casting", Metallurgical and Materials Transactions B, 1982, vol. 13B (June), p. 259.

APPENDIX A. FINITE ELEMENT IMPLEMENTATION OF HEAT TRANSFER MODEL

A. Linear Temperature Triangles

The small triangles in Figure 33 show the constant temperature-gradient triangle element used for the heat-flow model. Temperature within an element is interpolated by the same shape functions used to interpolate the coordinates.

$$T = \sum_{i=1}^{3} N_i(x, y) T_i \tag{50}$$

The $[B]$ matrix in global coordinate system can be obtained as:

$$[B] = \frac{1}{2A} \begin{bmatrix} y_2 - y_3 & y_3 - y_1 & y_1 - y_2 \\ x_3 - x_2 & x_1 - x_3 & x_2 - x_1 \end{bmatrix} \tag{51}$$

where A is the area of the triangle element.

B. *Conductance Matrix and Capacitance Matrix*

The element conductance and capacitance matrices needed to assemble Eq. [15] are given in Eqs. [52] and [53] [73].

$$[K]_{el} = \int [B]^T \begin{bmatrix} k_e & 0 \\ 0 & k_e \end{bmatrix} [B] dA \tag{52}$$

$$[C]_{el} = \int [N]^T \rho c_{pe} [N] dA = \frac{\rho c_{pe} A}{12} \begin{bmatrix} 2 & 1 & 1 \\ 1 & 2 & 1 \\ 1 & 1 & 2 \end{bmatrix} \tag{53}$$

k_e is the average conductivity of the three nodal values within each element and c_{pe} is the effective specific heat within the element, given by Eq. [16].

APPENDIX B. FINITE ELEMENT IMPLEMENTATION OF STRESS MODEL

A. Linear Strain Elements

Figure 33 shows the 6-node linear-strain isoparametric triangle finite element used in this work. Global coordinates and displacements within each element are interpolated from its nodal values by:

$$\begin{Bmatrix} x \\ y \end{Bmatrix} = \sum_{i=1}^{6} \begin{bmatrix} N_i & 0 \\ 0 & N_i \end{bmatrix} \begin{Bmatrix} x_i \\ y_i \end{Bmatrix} \tag{54}$$

$$\begin{Bmatrix} u \\ v \end{Bmatrix} = \sum_{i=1}^{6} \begin{bmatrix} N_i & 0 \\ 0 & N_i \end{bmatrix} \begin{Bmatrix} u_i \\ v_i \end{Bmatrix} \tag{55}$$

where the shape functions in natural local coordinates are

$$\begin{aligned} &[N_{i=1,2,\ldots,6}] = [s(2s-1) \quad t(2t-1) \quad r(2r-1) \quad 4st \quad 4tr \quad 4sr] \\ &r = 1 - s - t \end{aligned} \tag{56}$$

B. Generalized Plane Strain Formulation

The three unknowns, *a*, *b*, and *c*, which describe the out-of-plane strain in Eq. [5], are assembled into the finite element equations to be solved concurrently with in the in-plane displacements. The displacement vector is therefore:

$$\underset{15\times1}{\left\{\delta\right\}} = \left\{\underset{12\times1}{\left\{u\right\}}^T \quad a \quad b \quad c\right\}^T$$
$$\textit{where} \qquad [57]$$
$$\underset{12\times1}{\left\{u\right\}} = \left\{u_1 \quad \dots \quad u_6 \quad v_1 \quad \dots \quad v_6\right\}^T$$

The strain-displacement relationship is:

$$\left\{\Delta\varepsilon_x \quad \Delta\varepsilon_y \quad \Delta\varepsilon_{xy} \quad \Delta\varepsilon_z\right\}^T = \left[\underset{4\times15}{B'}\right]\left\{\delta\right\} \qquad [58]$$

The $\left[B'\right]$ for matrix generalized plane strain is given as:

$$\left[\underset{4\times15}{B'}\right] = \begin{bmatrix} \left[\underset{3\times12}{B}\right] & & \left[\underset{3\times3}{0}\right] & \\ \left[\underset{1\times12}{0}\right] & 1 & x & y \end{bmatrix}$$
$$\textit{where} \qquad [59]$$
$$\left[\underset{3\times12}{B}\right] = \begin{bmatrix} \frac{\partial N_1}{\partial x} & \cdots & \frac{\partial N_6}{\partial x} & 0 & \cdots & 0 \\ 0 & \cdots & 0 & \frac{\partial N_1}{\partial y} & \cdots & \frac{\partial N_6}{\partial y} \\ \frac{\partial N_1}{\partial y} & \cdots & \frac{\partial N_6}{\partial y} & \frac{\partial N_1}{\partial x} & \cdots & \frac{\partial N_6}{\partial x} \end{bmatrix}$$

The elastic stress-strain relation is:

$$\begin{Bmatrix} \Delta\sigma_x \\ \Delta\sigma_y \\ \Delta\sigma_{xy} \\ \Delta\sigma_z \end{Bmatrix} = \left[D\right]\left(\begin{Bmatrix} \Delta\varepsilon_x \\ \Delta\varepsilon_y \\ \Delta\varepsilon_{xy} \\ \Delta\varepsilon_z \end{Bmatrix} - \begin{Bmatrix} \Delta\varepsilon_T \\ \Delta\varepsilon_T \\ 0 \\ \Delta\varepsilon_T \end{Bmatrix} - \begin{Bmatrix} \Delta\varepsilon_{plx} \\ \Delta\varepsilon_{ply} \\ \Delta\varepsilon_{plxy} \\ \Delta\varepsilon_{plz} \end{Bmatrix} \right) \qquad [60]$$

The deviatoric stress vector is:

$$\left\{\sigma\right\}' = \left\{\sigma_x - \frac{1}{3}\sigma_m \quad \sigma_y - \frac{1}{3}\sigma_m \quad \sigma_z - \frac{1}{3}\sigma_m \quad \tau_{xy}\right\}$$
$$\textit{where} \qquad [61]$$
$$\sigma_m = \sigma_x + \sigma_y + \sigma_z$$

The von-Mises or "equivalent" stress is:

$$\bar{\sigma} = \sqrt{\frac{1}{2}\left(\left(\sigma_x - \sigma_y\right)^2 + \left(\sigma_x - \sigma_z\right)^2 + \left(\sigma_z - \sigma_y\right)^2 + 2\tau_{xy}^2\right)} \qquad [62]$$

C. Global Stiffness Matrix and Force Vectors

The global stiffness matrix $[K]$, and force vectors, $\{\Delta F_{\varepsilon_{th}}\}$, $\{\Delta F_{\varepsilon_{pl}}\}$, $\{F_{fp}\}$, and $\{F_{el}\}$ in Eq. [21] are assembled from the local stiffness matrix and force vectors of each element at the current time step $t+\Delta t$.

$$[K]=\sum_{e=1}^{n}\int_{A_e}\left([B]_e\right)^T[D][B]_e\,dA \qquad [63]$$

$$\{F_{fp}\}=\sum_{e=1}^{nb}\int_{L_{fp}}\left([N]_e\right)^T(F_p)dL_{fp} \qquad [64]$$

$$\{\Delta F_{th}\}=\sum_{e=1}^{n}\int_{A_e}\left([B]_e\right)^T[D]\{\Delta\varepsilon^{th}\}\,dA \qquad [65]$$

$$\{\Delta F_{in}\}=\sum_{e=1}^{n}\int_{A_e}\left([B]_e\right)^T[D]\{\Delta\varepsilon^{in}\}\,dA \qquad [66]$$

$$\{F_{el}\}=\sum_{e=1}^{n}\int_{A_e}\left([B]_e\right)^T[D]\{\varepsilon^{el}\}\,dA \qquad [67]$$

Integrals are evaluated numerically using standard 2nd order Gauss quadrature [74] according to the integration sampling points given in Figure 33 with a constant weighting factor of 1/3.

NOMENCLATURE

c_p	Specific heat of steel (kJ/kgK)
c	Sign of the equivalent stress/strain
E	Young's modulus (MPa)
F_p	Ferrostatic pressure
g	Gravity acceleration
H	Enthalpy of steel (kJ/kg)
k	Conductivity of steel (W/mK)
Nu	Nusselt Number
q	Heat flux
T	Temperature (^{o}C)
TLE	Thermal linear expansion
ΔT_B	brittle temperature range
u	Displacement (m)
v_c	Casting Speed
W	Mold Section Size

$\underset{\sim}{b}$	Body force vector
$[C]$	Capacitance matrix
$[D]$, $\underset{\approx}{D}$	Elasticity matrix/tensor
$\{F_{fp}\}$	Force vector due to ferrostatic pressure

$\{F_q\}$	Heat flow load vector
$[K]$	Conductance matrix for heat transfer model, Stiffness matrix for stress model
$\hat{n}$	Unit vector normal to the mold wall surface
$\{Q\}$	Heat generation vector
$\underset{\approx}{\varepsilon}, \{\varepsilon\}$	Strain tensor/vector
$\Delta\hat{\underset{\approx}{\varepsilon}}$	Estimated of total strain increment
$\underset{\approx}{\sigma}, \{\sigma\}$	Stress tensor/vector
$\underset{\approx}{\sigma}', \{\sigma\}'$	Deviatoric stress tensor/vector
$\underset{\approx}{\sigma}^*, \{\sigma\}^*$	Stress tensor/vector without inelastic increament components

α	Thermal expansion coefficient
ε	Strain
$\bar{\varepsilon}$	Equivalent strain
μ	Lame constant
ν	Poisson's ratio
ρ	Density of steel (kg/m^3)
$\bar{\sigma}$	Equivalent stress
σ_{yield}	Yield stress (MPa)

Subscripts

flow	Flow
in	Inelastic
th	Thermal
x	Component along x direction
y	Component along y direction
γ	Austenite
δ	δ-ferrite
ε	Elastic

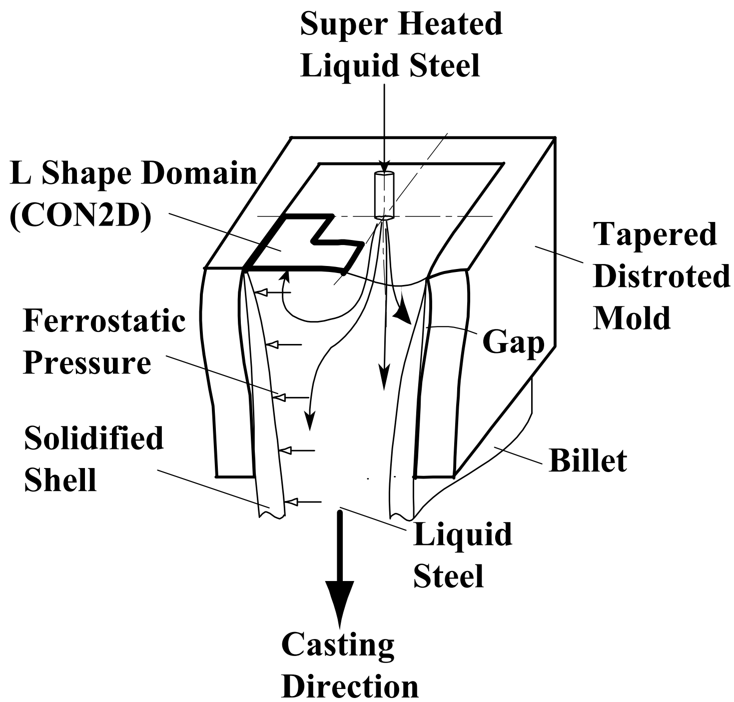

(a) Schematic of billet casting

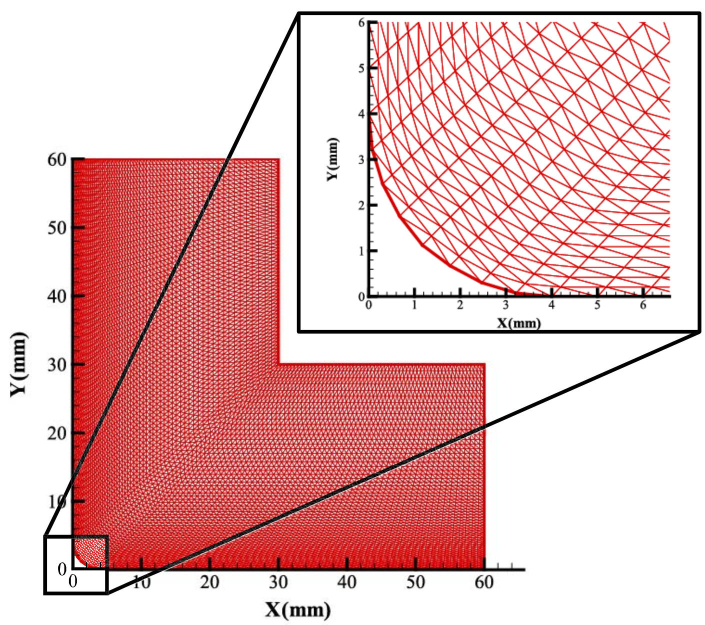

(b) L-shaped mesh of 3-node heat transfer elements (shown) connected into 6-node stress elements

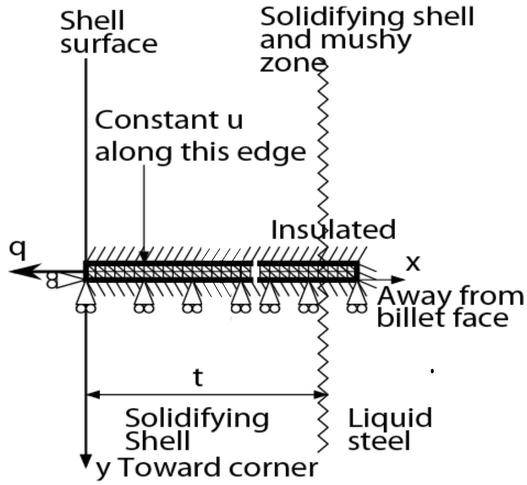

(c) Schematic of slice domain at the billet centerline

Fig. 1: Modeling domain of casting billet

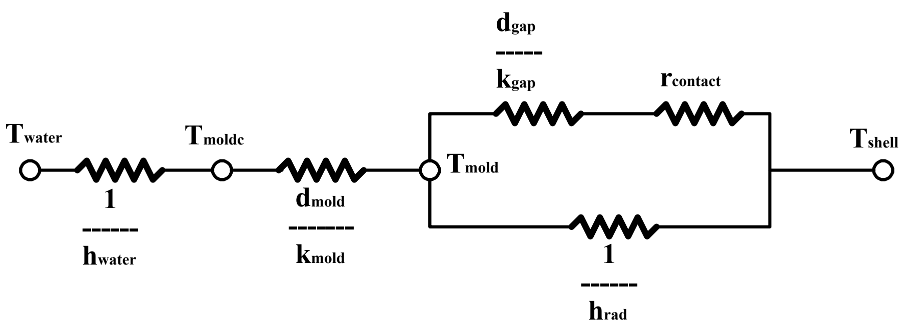

Fig. 2: Schematic of thermal resistor model of the interfacial layer between mold and billet

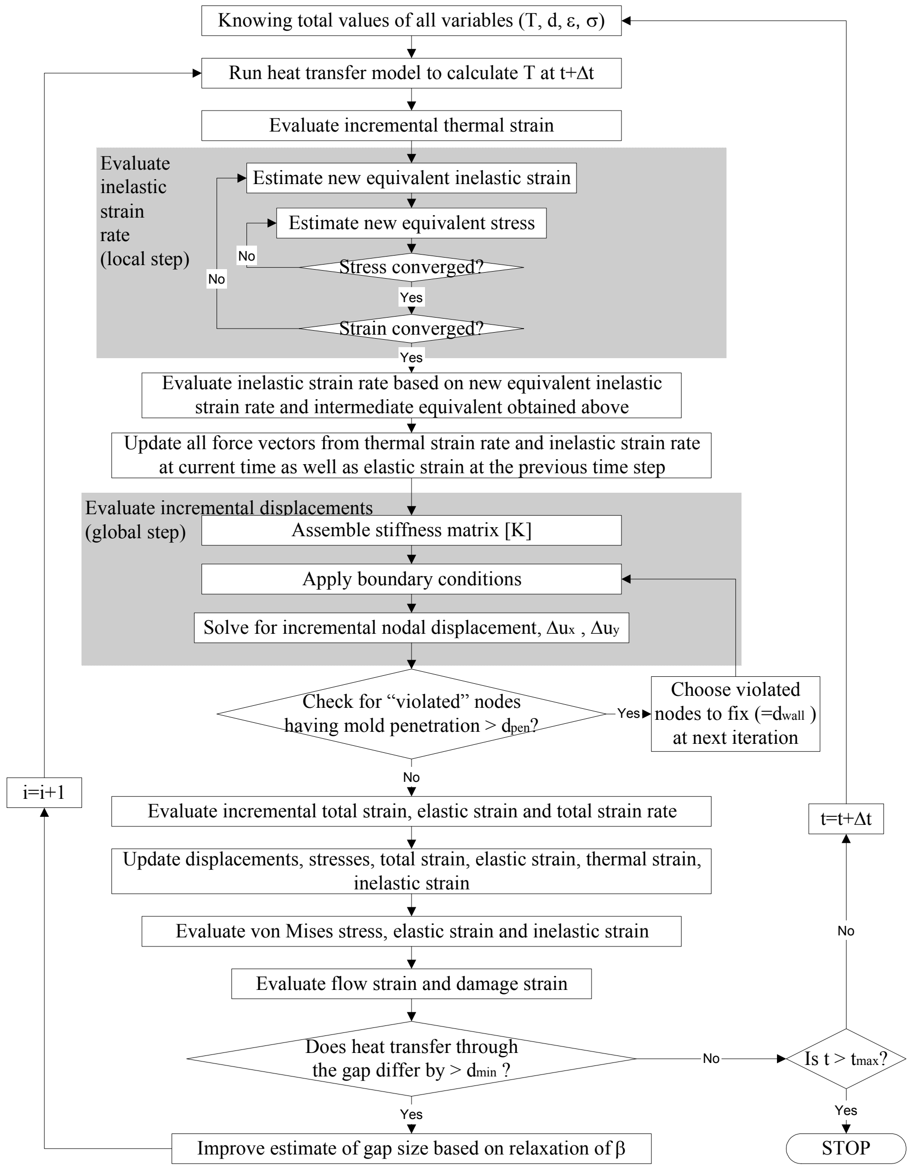

Fig. 3: Flow chart of CON2D

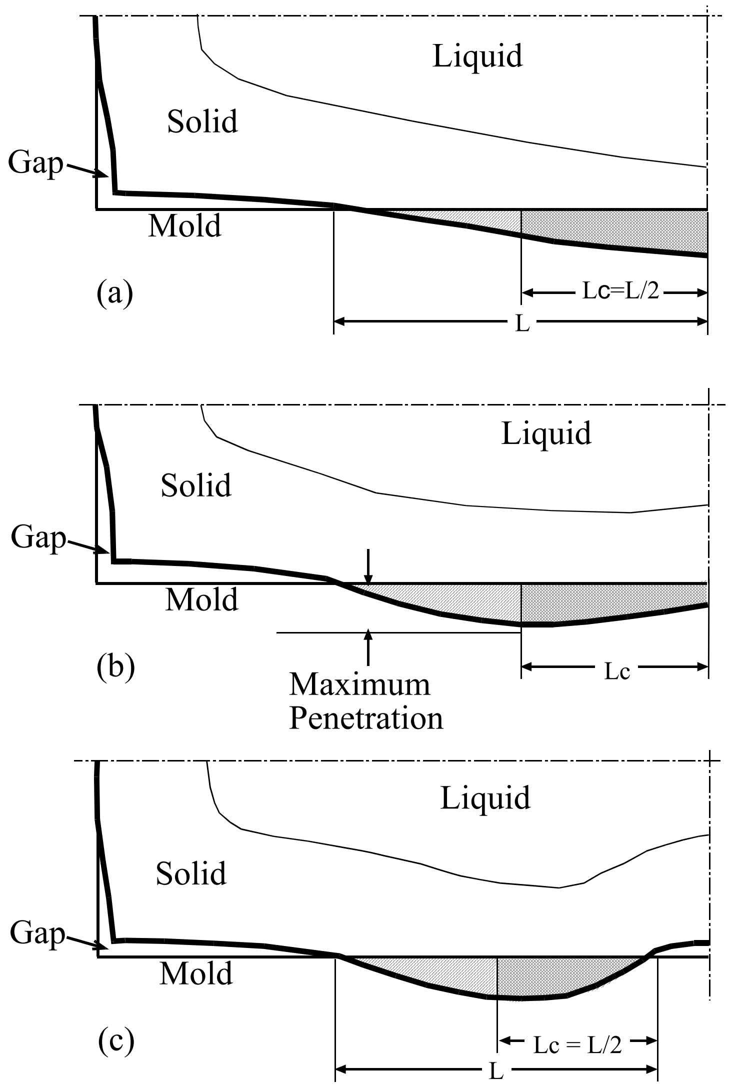

Fig. 4: Three types of penetration modes in contact algorithm

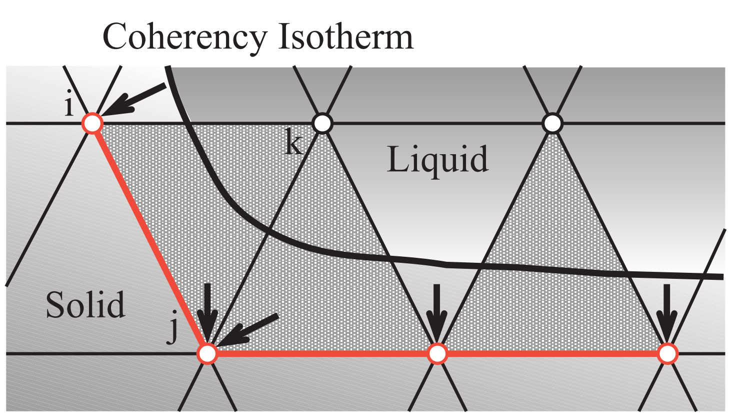

Fig. 5: Schematic of how ferrostatic pressure is applied at the internal boundary

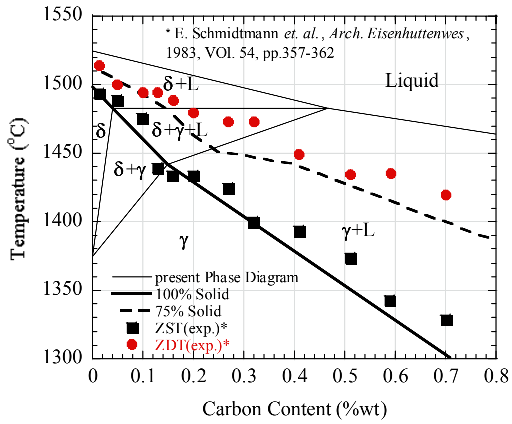

Fig. 6: Non-equilibrium Fe-C phase diagram[38] used in CON2D

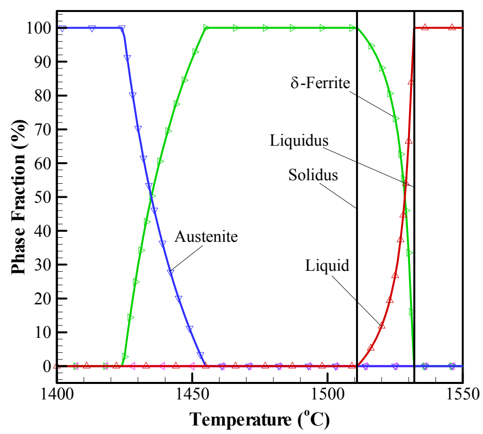

Fig. 7: Fraction as a function of temperature for the 0.04%C steel

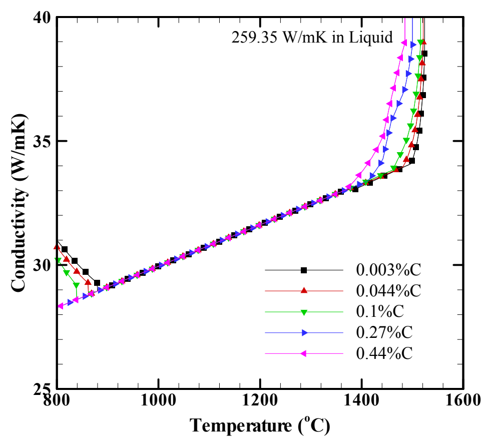

Fig. 8: Conductivity of plain carbon steels

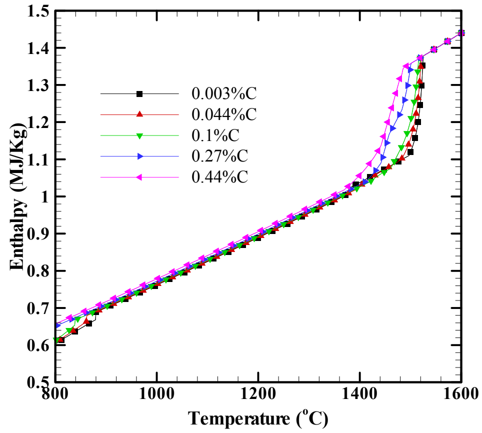

Fig. 9: Enthalpy of plain carbon steels

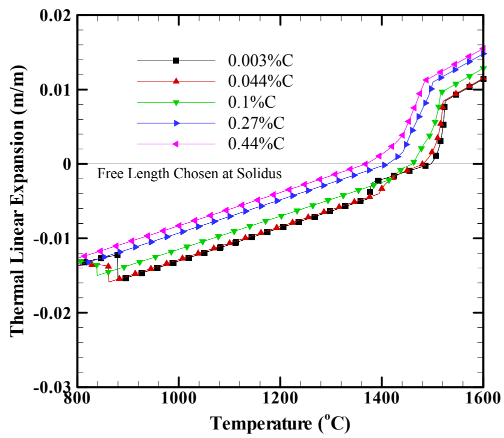

Fig. 10: Thermal linear expansion (TLE) of plain carbon steels

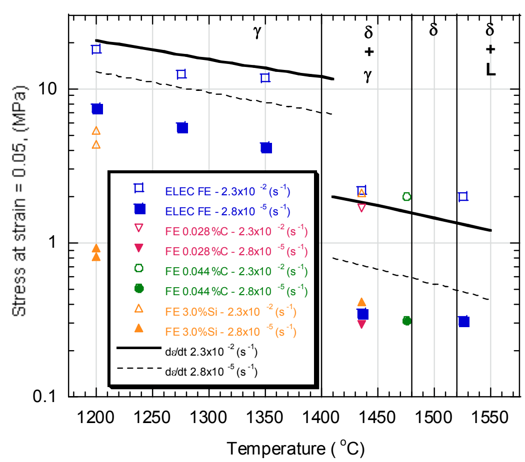

Fig. 11: Comparison of CON2D predicted and measured stress [62] at 5% plastic strain

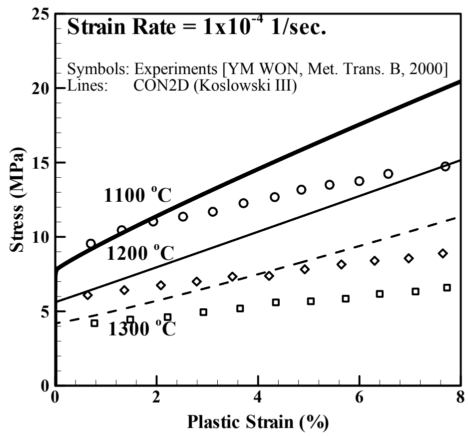

(a) Koslowski III law for austenite [61] against tensile test measurements [42]

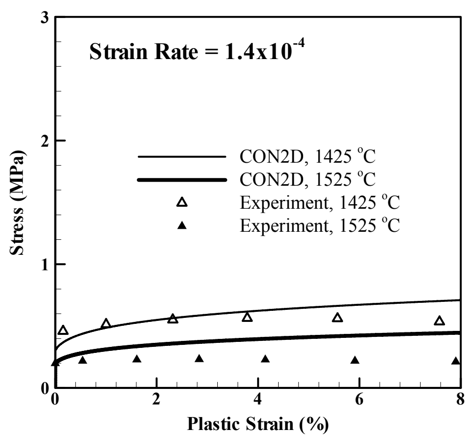

(b) Power law for δ-ferrite [3] against tensile test measurements [62]

Fig. 12: CON2D predictions compared with tensile-test measurements [42, 62]

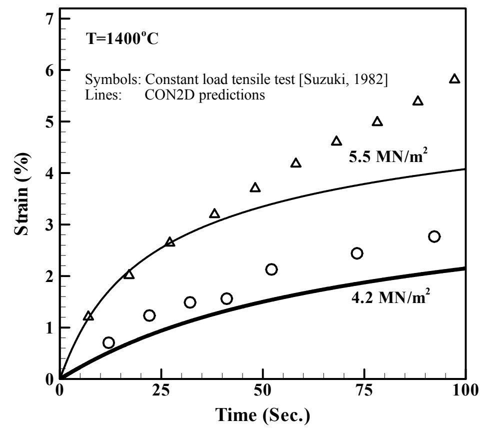

(a) Constant load

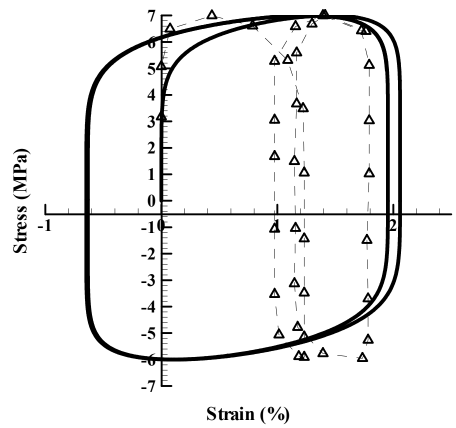

(b) Alternating load

Fig. 13: Predicted behavior of austenite compared with creep and cyclic loading test measurements at 1300 °C [64]

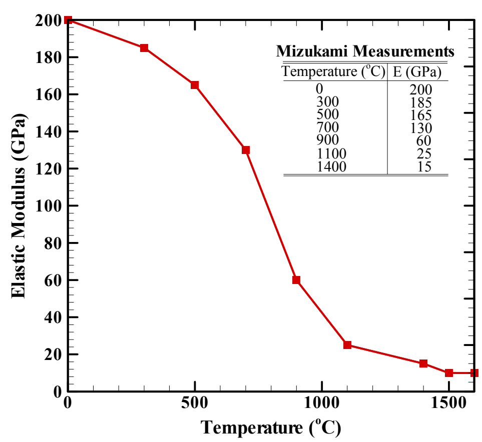

Fig. 14: Elastic modulus for plain carbon steels used in CON2D [65]

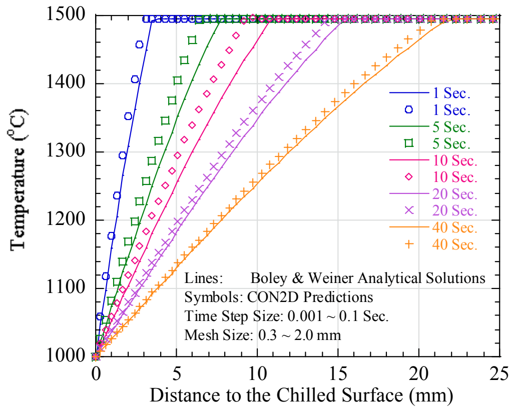

Fig. 15: Temperatures through an infinite solidifying plate at different solidification times compared with Boley & Weiner analytical solution

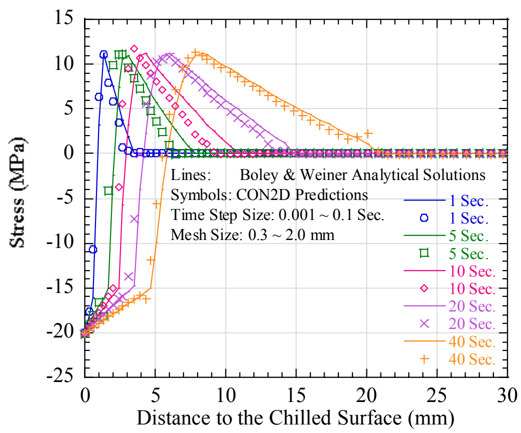

Fig. 16: Stresses through an infinite solidifying plate at different solidification times compared with Boley & Weiner analytical solution

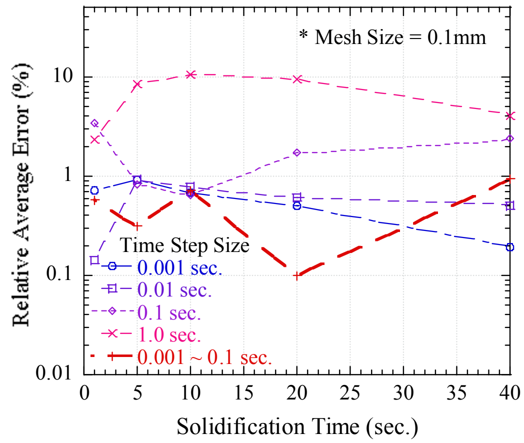

(a) Time step size effect

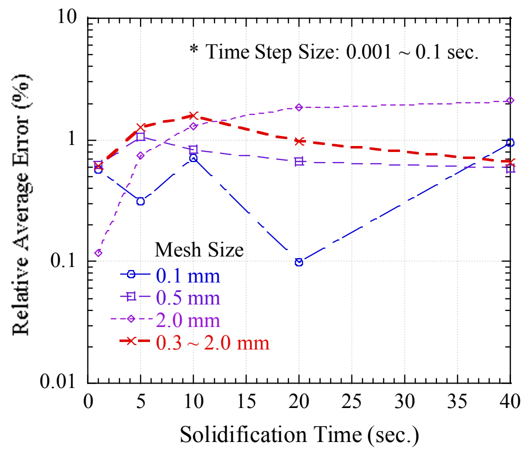

(b) Mesh size effect

Fig. 17: Temperature error between CON2D and analytical solution [67] from convergence studies

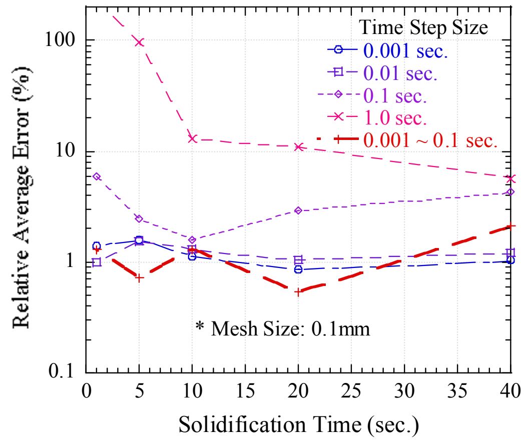

(a) Time step size effect

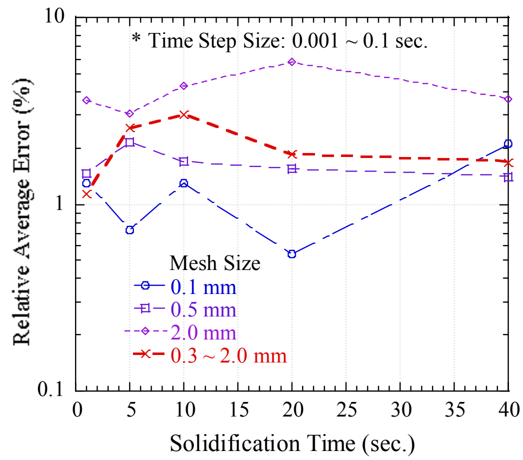

(b) Mesh size effect

Fig. 18: Stress error between CON2D and analytical solution [67] from convergence studies

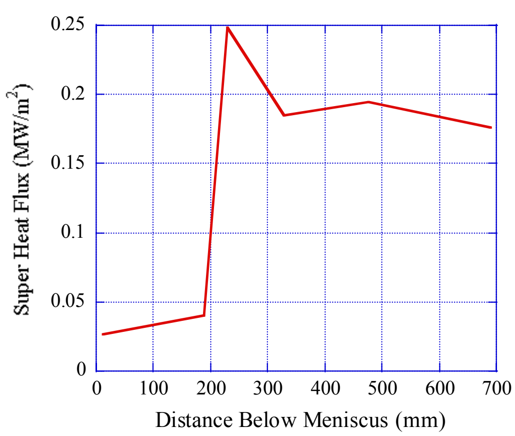

Fig. 19: Super heat flux used in CON2D for billet casting simulation

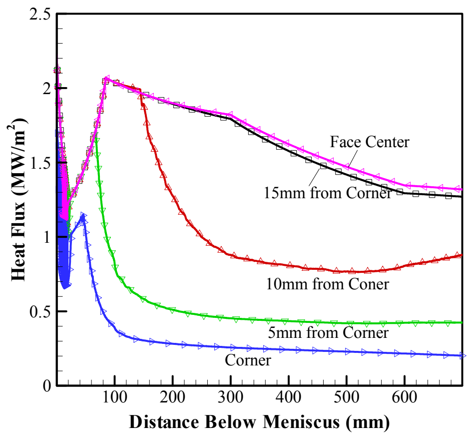

Fig. 20: Predicted instantaneous heat flux profiles in billet casting mold

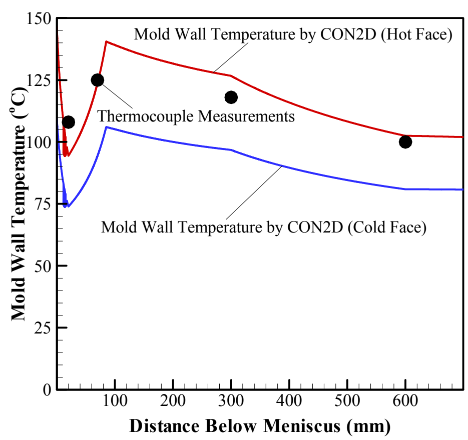

Fig. 21: Predicted mold wall temperature profiles compared with plant measurements

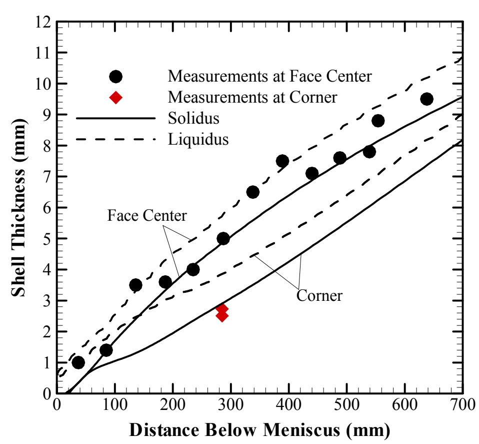

Fig. 22: Predicted shell thickness profiles for billet casting compared with plant measurements

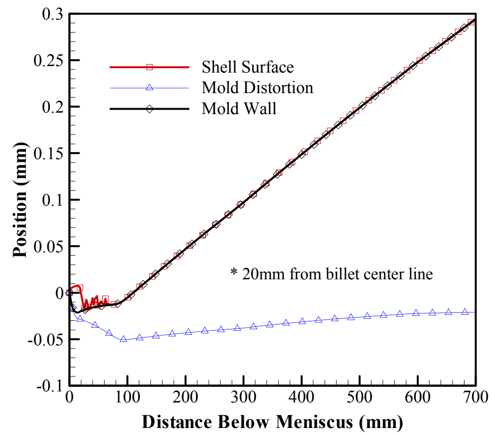

Fig. 23: Mold distortion, mold wall position and shell surface profiles for the billet casting simulation

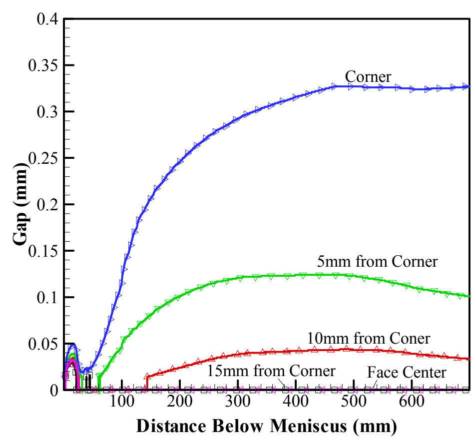

Fig. 24: Gap evolution predicted by CON2D for the billet casting simulation

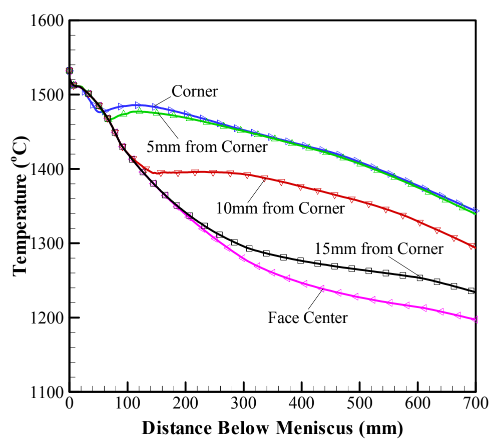

Fig. 25: Shell surface temperatures predicted for billet casting simulation

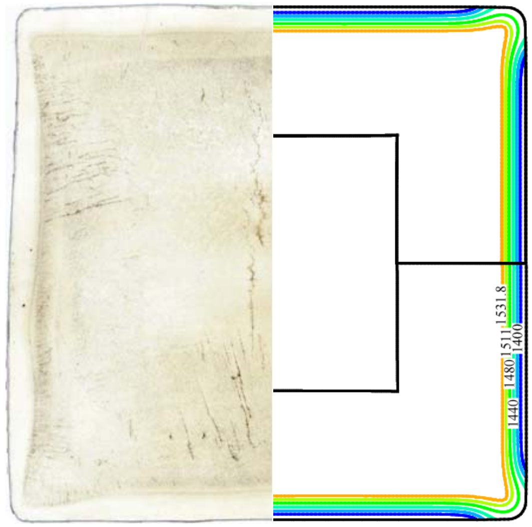

Fig. 26: Temperature contours at 285mm below meniscus compared with corresponding sulfur print from plant trial

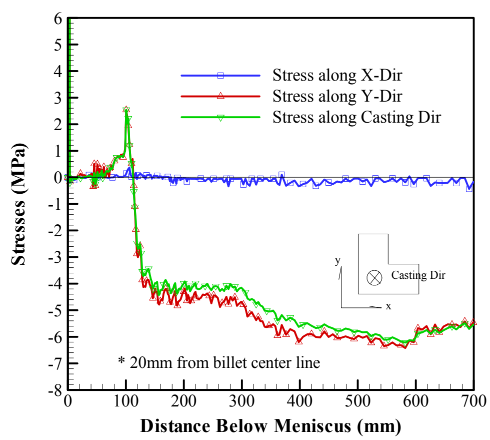

Fig. 27: Surface stress histories predicted near the billet face center (2-D L-mesh domain)

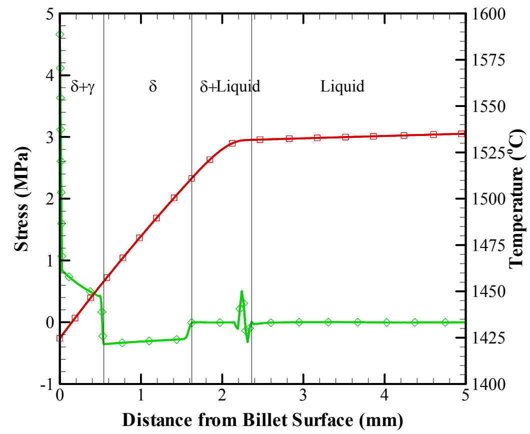

(a) 100 mm below meniscus

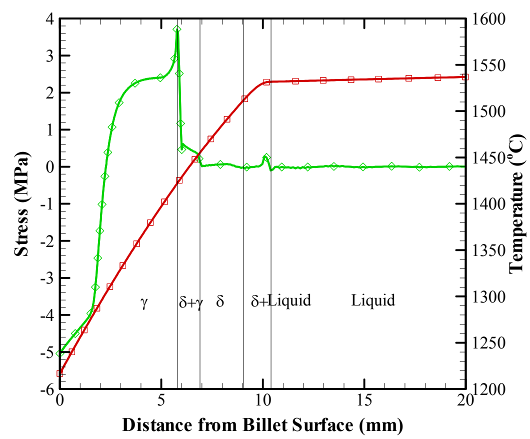

(b) Mold exit (700 mm below meniscus)

Fig. 28: Stress and temperature predicted through the shell thickness far from billet corner (slice domain)

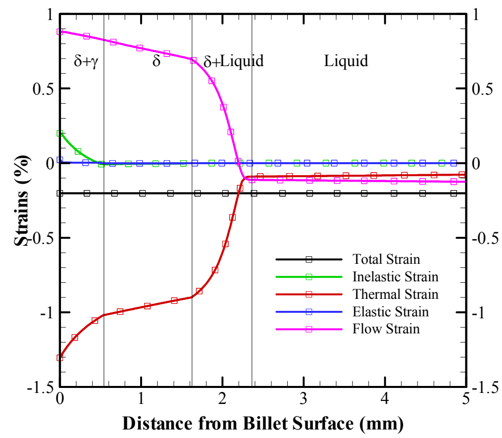

(a) 100 mm below meniscus

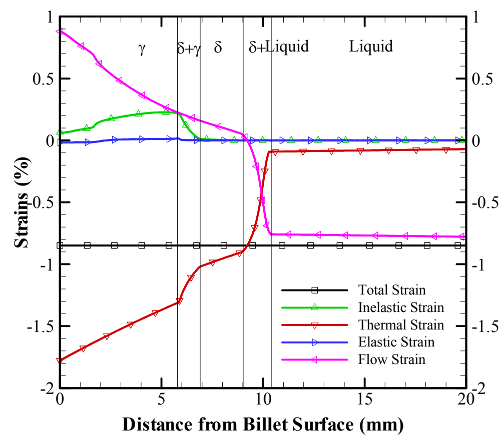

(b) Mold exit (700 mm below meniscus)

Fig. 29: Strain components predicted through the shell thickness far away from billet corner (slice domain)

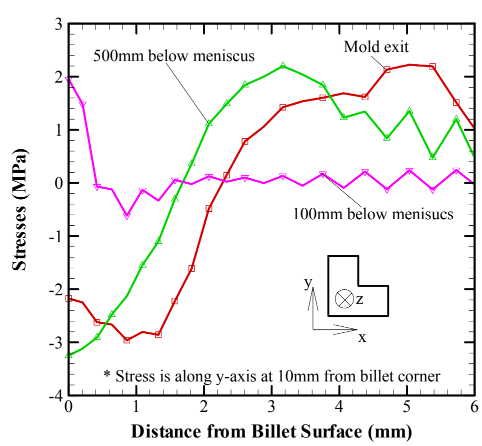

Fig. 30: Stress predicted through the shell thickness near billet corner (2-D L-mesh domain)

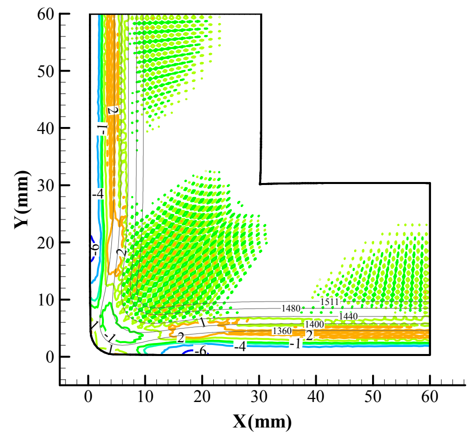

Fig. 31: Stress contours predicted at mold exit

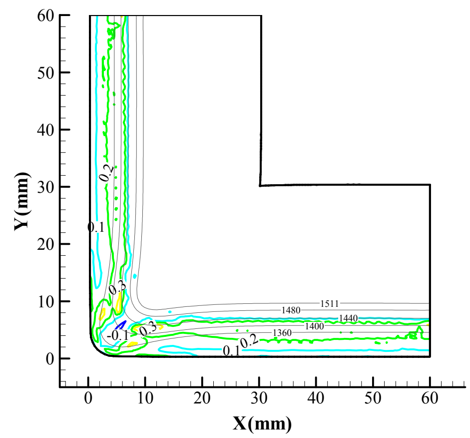

Fig. 32: Inelastic strain contours predicted at mold exit

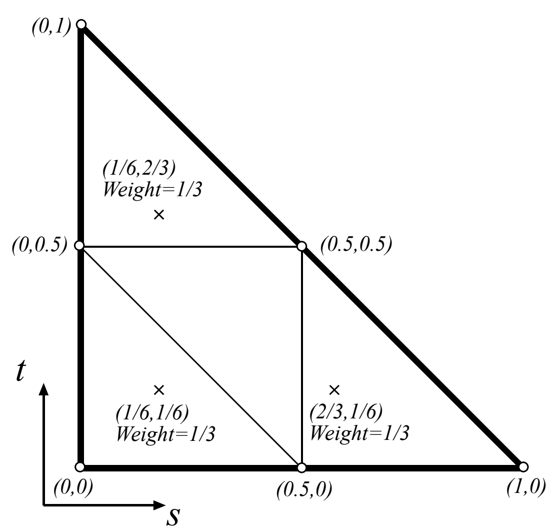

Fig. 33: 6-node quadratic displacement triangle element with Gauss points for stress model and corresponding four 3-node linear temperature triangle elements

Table I. Parameters of the interface model

Cooling Water Heat Transfer Coefficient, h_{water} (W/m^2K)	22,000 ~ 25,000
Cooling Water Temperature, T_{water} (^oC)	30 ~ 42
Mold Wall Thickness, d_{mold} (mm)	6
Mold Wall Conductivity, k_{mold} (W/mK)	360
Gap Conductivity, k_{gap} (W/mK)	0.02
Contact Resistance, $r_{contact}$ (m^2K/W)	6×10^{-4}
Mold Wall Emissivity	0.5
Steel Emissivity	0.8

Table II. Constants used in Boley and Weiner analytical solution

Conductivity (W/mK)	33.0
Specific Heat (kJ/kgK)	0.661
Latent Heat (kJ/kg)	272.0
Elastic Modulus in Solid (GPa)	40.0
Elastic Modulus in Liquid (GPa)	14.0
Thermal Linear Expansion Coefficient (1/K)	0.00002
Density (kg/m^3)	7500.0
Poisson's Ratio	0.3
Melting Temperature, T_{melt} (^oC)	1494.4
Liquidus Temperature (^oC)	1494.45
Solidus Temperature (^oC)	1494.35
Cold Surface Temperature, T_{cold} (^oC)	1000.0

Table III. Material details in billet plant trial

Steel Composition (wt%)	0.04C
Liquidus Temperature (^oC)	1532.1
70% Solid Temperature (^oC)	1525.2
90% Solid Temperature (^oC)	1518.9
Solidus Temperature (^oC)	1510.9
Austenite→α-Ferrite Starting Temperature (^oC)	781.36
Eutectoid Temperature (^oC)	711.22

Table IV. Simulation conditions in billet plant trial

Billet Section Size (mm×mm)	120×120
Working Mold Length (mm)	700
Total Mold Length (mm)	800
Casting speed (m/min)	2.2
Mold corner radius, (mm)	4
Taper (%m)	0.785 (on each face)
Time to turn on ferrostatic pressure (sec.)	2.5
Mesh Size (mm×mm)	0.1×0.1 - 1.4×1.0
Number of Nodes (varies with section size)	7381
Number of Elements (varies with section size)	7200
Time Step Size (sec.)	0.0001 - 0.005
Pouring Temperature (^oC)	1555.0
Coherency Temperature (^oC)	1510.9
Gap tolerance, d_{min}	0.001 (0.1%)
Minimum gap, d_{gapmin} (mm)	0.012
Penetration tolerance, d_{pen} (mm)	0.001